2003

Thermohydrodynamic analysis of compressible gas flow in compliant foil bearings

Zhengchun Peng
Louisiana State University and Agricultural and Mechanical College

THERMOHYDRODYNAMIC ANALYSIS OF COMPRESSIBLE GAS FLOW IN COMPLIANT FOIL BEARINGS

A Thesis

Submitted to the Graduate Faculty of the
Louisiana State University and
Agricultural and Mechanical College
in partial fulfillment of the
requirements for the degree of
Master of Science in Mechanical Engineering

in

The Department of Mechanical Engineering

by
Zhengchun Peng
B.S in Vehicle Engineering
Beijing Institute of Technology, China, 1996
May 2003

ACKNOWLEDGEMENTS

I am indebted to my research advisor, Dr. Michael Khonsari, who made possible my graduate study in US, for his invaluable, and in many times crucial, guidance throughout the course of this thesis work. He taught me from basic heat transfer to many what I would call the "subtle" fluids and tribological issues. Disregarded my "zero" background in computational fluid dynamics (CFD), he trusted me with challenging CFD task. He shone his learning to extend my wit in my study and gave his encouragement in my weakness. And most of all, I am indebted to him for his strict way of teaching me to be, more than just a serious researcher, a responsible person, without which I would have become different guy.

I give my gratitude to my committee member, Dr. Yitshak Ram, with whom I took several graduate courses and founded my confidence in research of not just one field. I am thankful to Dr. Wen-Jin Meng, also my committee member, for his support and spending time in evaluating my thesis and being my good example in his profession.

Dr. James Barber, a prominent professor from Mechanical Engineering department at University of Michigan, who spent his time on part of my research and advised me through precious correspondence, has my best regards.

I also thank Dr. Michael Murphy, who supported me in teaching and grading a big class of undergraduate students for a year and half, for spending his time on my questions from the fundamental to his own unknowns. He has my respect and trust.

My friends in Dr. Khonsari's group, particularly Dr. J-Y. Jang, friendly helped and extensively discussed many aspects of my research, thank you all. Diane Morgan, "mother hen" of the Mechanical Engineering department, and Marie Hershey, my spoken

English teacher, helped me with unexpected kindnesses that I had not done, and probably will not do, anything to merit.

I am fortunate to have an excellent brother, Zhihui Peng, who is now a Ph.D student in the Chemistry department at University of California, Irvine and will join MERCK Corporation's R&D in 2003. His excellence and personal support has been my encouraging source for years in my study.

The most, I owe my parents, who could not be better supportive emotionally, a great deal amount of time in caring, even chatting, for return.

Last but not least, a portion of this work was funded by the Louisiana Space Consortium under the "seed" research project category of Unsolicited Research Proposal.

TABLE OF CONTENTS

LIST OF TABLES

LIST OF FIGURES

NOMENCLATURE

a	viscosity constant of air (N.s/K-m^2)
c_p	specific heat of gas (J/kg.K)
e	eccentricity (m)
h	fluid film thickness (m)
h_{conv}	heat transfer coefficient
k	conductivity of gas (W/k·m)
k_B	conductivity of top foil (W/k·m)
l	half of bump length (m)
p	hydrodynamic pressure (Pa)
p_a	ambient pressure (Pa)
q	heat flux (W/m^2)
r	cylindrical coordinate across the film thickness
s	bump pitch (m)
t_B	thickness of bushing or top foil (m)
t_{BF}	bump foil thickness (m)
u	linear velocity of gas flow in x direction (m/s) for Cartesian coordinate and in θ direction for Cylindrical coordinate
v	linear velocity of gas flow in axial, y, direction (m/s)
w	linear velocity of gas flow in z direction (m/s) for Cartesian coordinate and in r direction for Cylindrical coordinate
x	Cartesian coordinate in the direction of motion
y	coordinate in axial direction
z	Cartesian coordinate across the film thickness

C	radial clearance (m)
D	bearing diameter (m)
E	Yong's modulus of bump foil
K_{BC}	bump foil compliance (m^3/E)
K_{BS}	bump foil stiffness (E/m)
L	bearing length (m)
R	shaft radius (m)
Q_{leak}	leak flow rate (kg/s)
Q_{rec}	re-circulate flow rate (kg/s)
T	temperature of gas (K)
T_{ref}	reference temperature (K)
T_i	"inlet" temperature of the gas film (K)
T_s	shaft temperature (K)
T_B	temperature of bushing or top foil (K)
U	linear velocity of shaft speed (m/s)
W	load (N)
α	bump foil compliance number
ε	eccentricity ratio
ρ	gas density (kg/m^3)
ρ_0	S.P.T. gas density (kg/m^3)
μ	fluid viscosity ($N.s/m^2$)
μ_0	ambient viscosity of gas ($N.s/m^2$)
ν	Poisson's ratio of bump foil
ω	shaft angular speed (rpm)

θ cylindrical coordinate in the direction of motion

Λ bearing number (or compressibility number)

Φ viscous dissipation (N/m-s)

ABSTRACT

This thesis deals with the development of mathematical models and numerical schemes for simulating the hydrodynamic pressure and temperature rise of compliant foil bearings lubricated by a thin gas film in between its compliant bearing surface and the rotating shaft. The model accounts for the compressibility of gas, the compliance of the bearing surface, and the interaction between the pressure field and temperature field of the gas film in the bearing system. Numerical solutions obtained over a fairly large range of operating speeds show excellent agreement with existing experimental data from both load performance test and bearing temperature measurement.

A series of parametric study is presented to illustrate the utility of the developed algorithms for characterization of foil bearing performance using both isothermal and thermohydrodynamic theories. The numerical algorithm can handle high speeds and high eccentricity ratios, which allows the prediction of realistic performance and characteristics of foil bearings under extreme operating conditions.

CHAPTER1. INTRODUCTION

Applications of air-lubricated foil bearing have been under extensive investigation by NASA Glenn Research Center for the so-called oil-free turbine engines. For example, the investigation on their use in automotive gas turbine engines has been identified as a revolutionary concept to realize a significant improvement in speed, efficiency, and reliability of turbine engines. Implementation of this enabling technology is expected to result in a significant weight reduction of turbomachinery with lower maintenance requirements, by eliminating the conventional lubricant supply system with its associated piping arrangements. In addition, air is an environmentally benign lubricant and is capable of accommodating operation at elevated temperatures, whereas conventional oil-lubricated bearings fail because the oil viscosity drops exponentially with increasing temperature.

The use of foil gas bearings is common in lightly-loaded, low temperature applications ranging from the magnetic disk drive read/write heads in PCs to the air cycle machines (ACM) in aircrafts. But recent advances in foil bearing designs have embarked many new applications in advanced rotating machinery. In particular, the new generations of foil bearings have much greater load-carrying capacity and operating temperature limits. For example, Heshmat [1] demonstrated an advanced design of a foil bearing (D=35mm and L=31mm) that achieved a breakthrough load-carrying capacity of 670,000 Pa at 59,700 rpm. DellaCorte [2] reported a series of performance data of foil bearings operating up to 700°C.

The configuration of a foil bearing is shown in Fig.1. It is comprised of a cylindrical shell (sleeve) lined with corrugated bumps (bump foil) topped with a thin, flat

foil (top foil). The ambient air provides the necessary lubrication after startup. When the shaft rotates over a certain angular speed, it draws air in between the top foil and the shaft and forms a protective air film which completely separates them apart. With an air film maintained between the rotating and stationary surfaces, an adequate pressure is generated which bears the applied load. The bump foil provides support for the top foil and its compliant feature allows the top foil to deform under the action of hydrodynamic pressure.

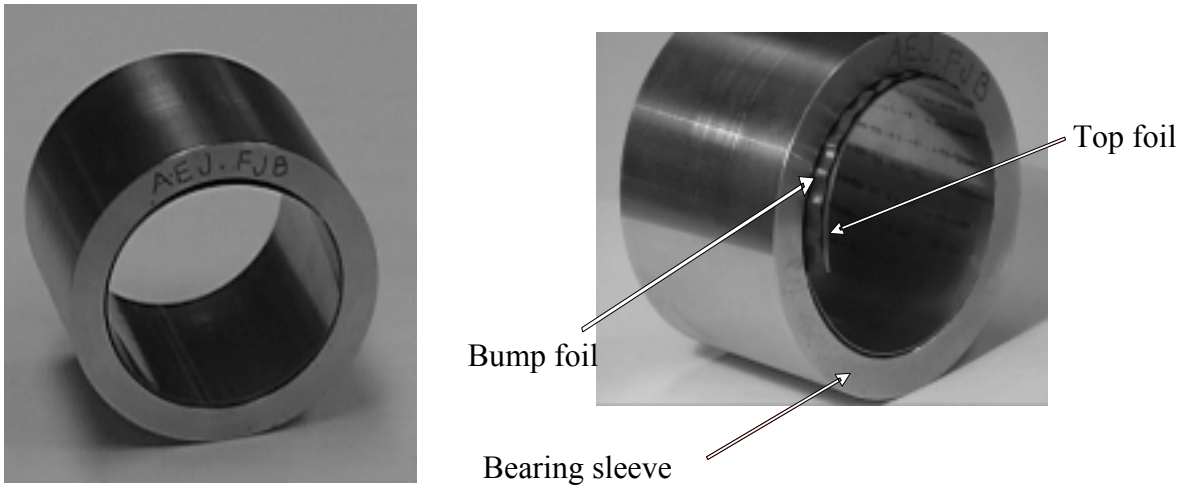

Fig. 1 Pictures of a foil bearing (NASA property s/n AEJ. FJB)

Nevertheless, foil bearings are not without disadvantages. Three serious drawbacks that prevent foil bearings from widespread use are: i) comparing to their oil-lubricated counterparts, they can sustain a much less load-carrying capacity; ii) the bearing surface (top foil) is susceptible to damage during start/stop cycling [3]; iii) their performance characteristics are not well understood. The first drawback is because of the air viscosity is inherently low; the second disadvantage is because there is no gas film formed as the lubricant at the start/stop stages; and the third obstacle is due to the

modeling difficulties as a consequence of the fact that the foil bearings are nonlinear both structurally and hydrodynamically [4]. The interactions between hydrodynamic film pressure and foil compliance, lubricant film properties (e.g., viscosity and density) and viscous heat generation, and foil mechanical properties and operating temperature add even more difficulties to a reliable prediction of foil bearings performance.

Research is needed to overcome these hurdles. Innovative designs based on optimization of bump stiffness and elastic-hydrodynamic analytical modeling of foil bearing structures have made significant progress in improving the load-carrying capacity of foil bearings [1,4,5]. Solid-lubricant coating for wear protection has been demonstrated to be effective during start-up and shutdown operation, thereby improving bearing life [6]. The third hurdle has not been overcome yet [4].

It is the aim of this thesis to focus on the modeling and simulation of the nonlinear behavior of gas flow in foil bearings and the related operational characteristics of these bearings. We report the development of a model that can be used to simulate realistic hydrodynamic pressure, operating lubricant-film profile and temperature field of foil bearings. Using this model, we present a series of foil bearing performance prediction over a large range of operating speeds. This information is needed to better understand the operational characteristics of foil bearings. It can also be helpful for the purpose of designing new generations of foil bearings.

CHAPTER2. THEORY

Prediction of the hydrodynamic pressure of a foil bearing requires solving a non-linear partial differential equation known as the Reynolds equation. Once the pressure distribution is evaluated, the fluid velocity profile can be predicted. This information is, then, fed into the appropriate energy equation to determine the temperature field. This type of a problem is often referred to as the thermohydrodynamic analysis (THD). In a THD analysis dealing with an incompressible fluid the energy equation and the Reynolds equation are coupled through the lubricant's viscosity-temperature relationship. These interdependences require simultaneous treatment of both equations to arrive at a final solution for pressure and temperature. In a gas lubricated bearing there are additional couplings through the fluid's density and the pressure work, because of the gas compressibility. A proper THD analysis of a foil bearing must also account for the interaction between hydrodynamic pressure and foil compliance. Under the action of hydrodynamic pressure, the foil deforms and this causes an appreciable change in the film geometry. Therefore, the film thickness for both the Reynolds equation and the energy equation depend not only on the designed clearance and operating eccentricity, but also the deformation of the foils during operation.

A simplified numerical procedure for obtaining the simultaneous solutions to the coupled governing equations is represented by a flow chart in Fig. 2.

2.1 Compressible Reynolds' Equation

Shown in Fig. 3 is a journal bearing. The functional form of the film thickness is

$$h = C + e\cos\theta \tag{2.1.1}$$

where C is the radial clearance, θ is circumferential coordinate, and e is the eccentricity.

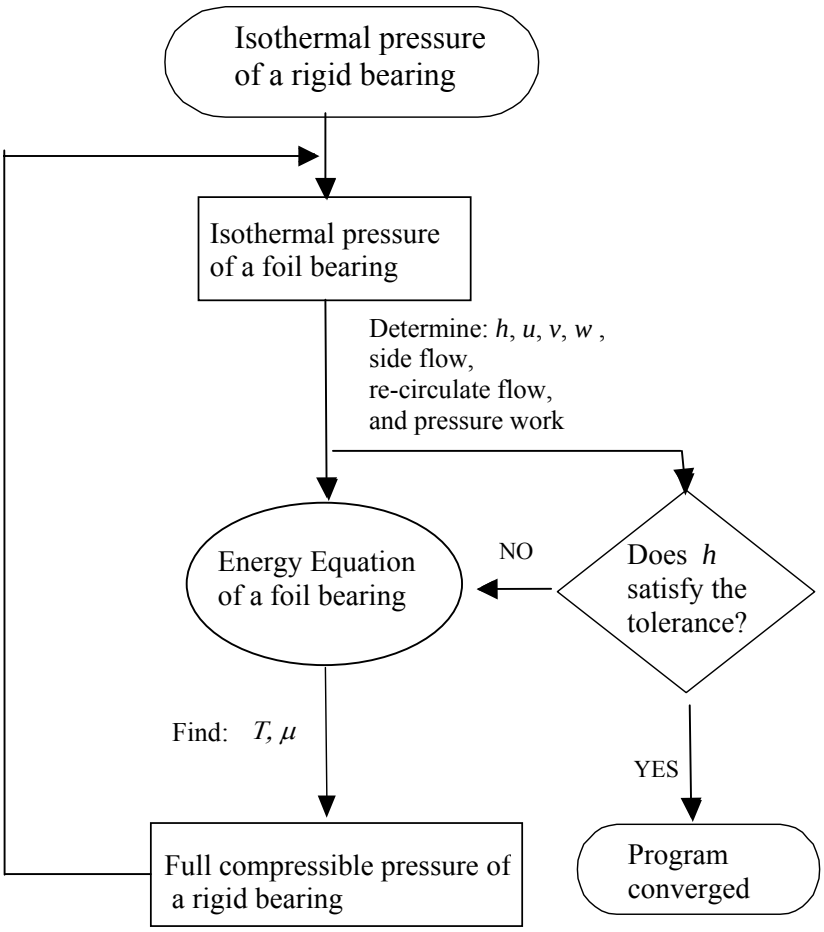

Fig. 2 The flow chart of THD analysis for foil bearings

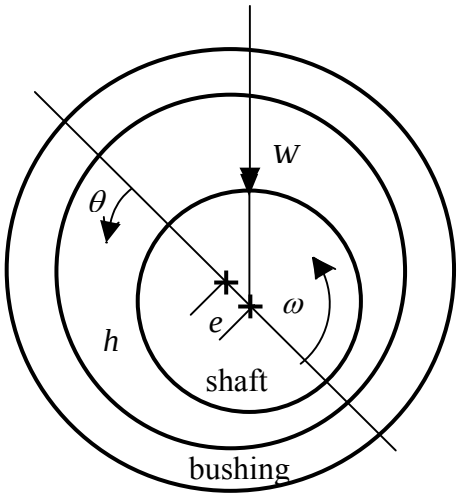

Fig. 3 Schematic of a journal bearing

Hydrodynamic pressure is built up in the convergent region of the lubricant film from h_{max}, where $\theta = 0$, to h_{min} along the circumferential direction when the journal rotates. In the divergent region, the hydrodynamic pressure decreases from the maximum pressure to satisfies the periodic boundary condition at the bearing end where $\theta = 360$. Since gas is compressible, a proper hydrodynamic analysis of gas bearing must account for the compressibility of the gas. The governing equation for pressure of a journal type bearing is given by the following compressible Reynolds equation:

$$\frac{1}{R^2}\frac{\partial}{\partial\theta}\left(\frac{\rho h^3}{12\mu}\frac{\partial p}{\partial\theta}\right)+\frac{\partial}{\partial y}\left(\frac{\rho h^3}{12\mu}\frac{\partial p}{\partial y}\right)=\frac{\omega}{2}\frac{d}{d\theta}(\rho h) \tag{2.1.2}$$

Assuming that the fluid is an ideal gas flow, Eq. (2.1.2) reads:

$$\frac{1}{R^2}\frac{\partial}{\partial\theta}\left(\frac{ph^3}{12\mu T}\frac{\partial p}{\partial\theta}\right)+\frac{\partial}{\partial y}\left(\frac{ph^3}{12\mu T}\frac{\partial p}{\partial y}\right)=\frac{\omega}{2}\frac{\partial}{\partial\theta}\left(\frac{ph}{T}\right) \tag{2.1.3}$$

Normalizing equation (2.1.3) yields

$$\frac{\partial}{\partial\theta}\left(\frac{\bar{p}\bar{h}^3}{\bar{\mu}\bar{T}}\frac{\partial\bar{p}}{\partial\theta}\right)+\left(\frac{D}{L}\right)^2\frac{\partial}{\partial\bar{y}}\left(\frac{\bar{p}\bar{h}^3}{\bar{\mu}\bar{T}}\frac{\partial\bar{p}}{\partial\bar{y}}\right)=\Lambda\frac{\partial}{\partial\theta}\left(\frac{\bar{p}\bar{h}}{\bar{T}}\right) \tag{2.1.4}$$

where

$$\bar{y}=\frac{y}{L/2},\ \bar{p}=\frac{p}{p_a},\ \bar{h}=\frac{h}{C},\ \bar{\mu}=\frac{\mu}{\mu_0},\ \bar{T}=\frac{T}{T_0}$$

and

$$\Lambda=\frac{6\mu_0\omega}{p_a}\left(\frac{R}{C}\right)^2 \tag{2.1.5}$$

Λ is the so-called bearing number or compressibility number.

Under the isothermal condition, Eq.(2.1.4) reduces to:

$$\frac{\partial}{\partial\theta}(\bar{p}\bar{h}^3\frac{\partial\bar{p}}{\partial\theta})+\left(\frac{D}{L}\right)^2\frac{\partial}{\partial\bar{y}}(\bar{p}\bar{h}^3\frac{\partial\bar{p}}{\partial\bar{y}})=\bar{\mu}\Lambda\frac{\partial}{\partial\theta}(\bar{p}\bar{h}) \tag{2.1.6}$$

In the foil bearing application, the bearing surface becomes compliant and the pressure directly affects the film thickness, *h*. A schematic of a foil bearing is depicted in Fig. 3. Fig.3 also illustrates the details of the foil structure, including a smooth top foil and a corrugated bump foil.

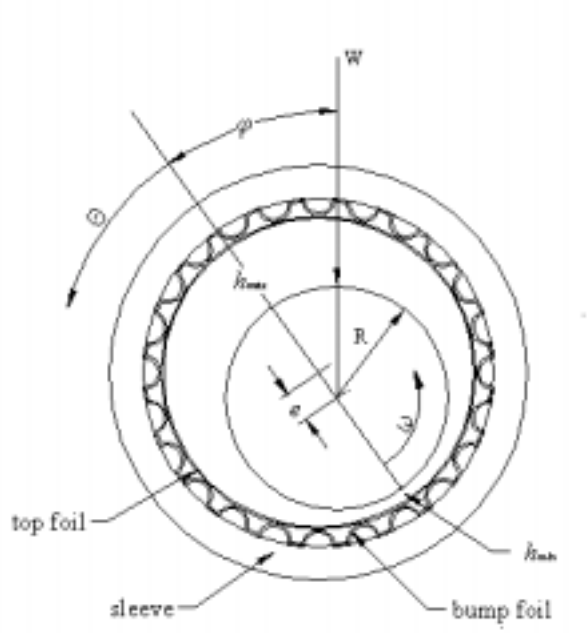

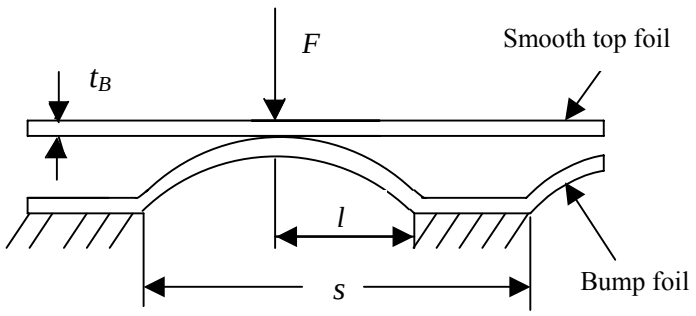

Fig. 4 Schematic of a foil bearing and detailed configuration of the foils

The compliance of the bump foil, with the geometry specified in Fig. 4, is determined by Heshmat [7] as:

$$K_{BC} = \frac{2s}{E}\left(\frac{l}{t_b}\right)^3 \left(1-\nu^2\right) \tag{2.1.7}$$

where s is the bump pitch, l is half of the bump length, t_b is the bump foil thickness, E and ν are the Young's modulus and Poisson's ratio of bump foil material, respectively. Accordingly, the film thickness, h, as a function of pressure, p, is given (see [7]):

$$h = C + e\cos\theta + K_1(p - p_a) \tag{2.1.8}$$

In dimensionless form, Eq. (2.1.8) reads:

$$\bar{h} = 1 + \varepsilon\cos\theta + \alpha(\bar{p} - 1) \tag{2.1.9}$$

where α is the so-called compliance number defined as:

$$\alpha = \frac{2p_a s}{CE}\left(\frac{l}{t_b}\right)^3 (1-\nu^2) \tag{2.1.10}$$

Note that in Eq. (2.1.9) there are two varying factors that determine the operating film geometry of a foil bearing: one is the deformation of the top foil under hydrodynamic pressure; the other is the eccentricity ratio, ε. A very peculiar phenomenon in foil bearing is that, according to Eq. (2.1.9), it allows for eccentricity ratio, ε, to be greater than 1, while maintaining a positive minimum film thickness. This is so because as the pressure deforms the top foil, it leaves a larger room than original clearance for shaft to move towards the minimum film thickness h_{min}.

For the first generation of foil bearings, a single bump layer is used. Therefore, the deformation of top foil and that the film thickness is not a function of axial direction,

y. Consequently, the arithmetic mean pressure in axial direction shall be used to calculate the top foil deformation. In this case, Eq. (2.1.6) reduces to:

$$\frac{\partial}{\partial\theta}(\bar{p}\bar{h}^3\frac{\partial\bar{p}}{\partial\theta})+\left(\frac{D}{L}\right)^2\bar{h}^3\frac{\partial}{\partial\bar{y}}(\bar{p}\frac{\partial\bar{p}}{\partial\bar{y}})=\bar{\mu}\Lambda\frac{\partial}{\partial\theta}(\bar{p}\bar{h}) \tag{2.1.11}$$

The appropriate boundary conditions for the Reynolds' equation are:

$$\begin{aligned}&\bar{p}=1 \quad \text{at} \quad \bar{y}=\pm 1\\ &\bar{p}(\theta=0)=\bar{p}(\theta=2\pi)\end{aligned} \tag{2.1.12}$$

The pressure field is symmetric about the bearing mid-plane. For computational efficiency, we calculate only half of the pressure field. In this case, the boundary condition becomes:

$$\begin{aligned}&\bar{p}=1 \quad \text{at} \quad \bar{y}=-1;\\ &\frac{\partial\bar{p}}{\partial\bar{y}}=0 \quad \text{at} \quad \bar{y}=0;\\ &\bar{p}(\theta=0)=\bar{p}(\theta=2\pi)\end{aligned} \tag{2.1.13}$$

Schematic load-carrying capacity and attitude angle calculation is shown in Fig. 5.

According to Khonsari and Booser [8],

$$\begin{aligned}\overline{W_x}&=\int_{-L/2}^{L/2}\int_0^{\theta_p}\bar{p}\cos\theta\,d\theta\,dy\\ \overline{W_y}&=\int_{-L/2}^{L/2}\int_0^{\theta_p}\bar{p}\sin\theta\,d\theta\,dy\end{aligned} \tag{2.1.14}$$

where $\overline{W_x}$ and $\overline{W_y}$ are the dimensionless load component along the line of centers and the line perpendicular to the line of the centers, respectively, and θ_p signifies the maximum angle of positive hydrodynamic pressure.

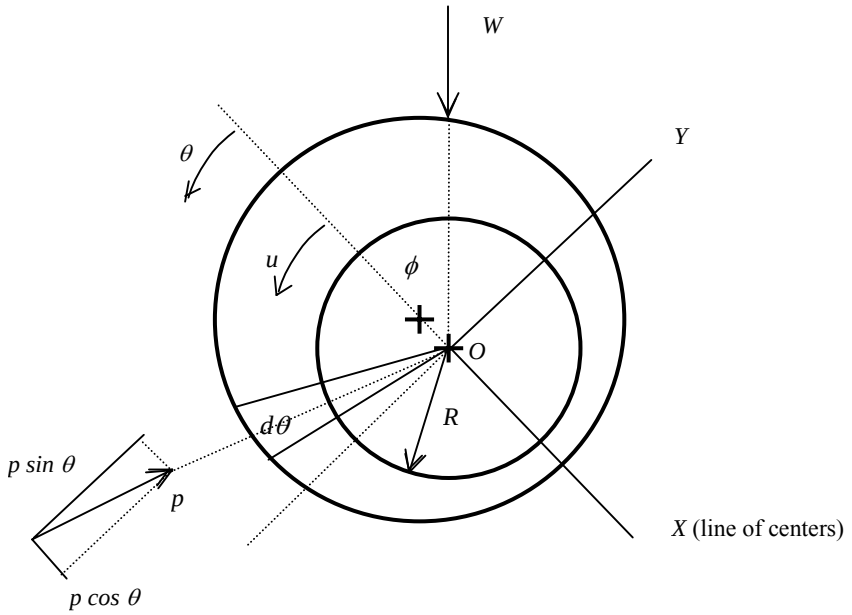

Fig. 5 Schematic of load-carrying capacity and attitude angle

The total load-carrying capacity is given by:

$$\overline{W} = \sqrt{\overline{W}_x^2 + \overline{W}_y^2} \tag{2.1.15}$$

where $\overline{W} = \dfrac{W}{p_a R}$.

The attitude angle is,

$$\tan\phi = \frac{\overline{W}_y}{\overline{W}_x} \tag{2.1.16}$$

2.2 Limiting Solutions to the Compressible Reynolds' Equation

Before solving the non-linear differential equation, Eq. (2.1.11), two limiting cases are investigated first.

Case 1: Low bearing numbers ($\Lambda \to 0$)

When the bearing speed ω is small and $\Lambda \to 0$, $\bar{p} \to 1$ and the pressure rise $\Delta\bar{p} \to 0$. According to Hamrock [9], we have

$$\left(\frac{\partial \bar{p}}{\partial \theta}\right)^2 << \frac{\partial^2 \bar{p}}{\partial \theta^2}$$

$$\left(\frac{\partial \bar{p}}{\partial \theta}\right)^2 << \frac{\partial^2 \bar{p}}{\partial \theta^2} \tag{2.2.1}$$

$$\bar{h}\frac{\partial \bar{p}}{\partial \theta} << \bar{p}\frac{\partial \bar{h}}{\partial \theta}$$

therefore, Eq.(2.1.11) reduces to:

$$\frac{\partial}{\partial \theta}\left(\bar{h}^3 \frac{\partial \bar{p}}{\partial \theta}\right) + \left(\frac{D}{L}\right)^2 \bar{h}^3 \frac{\partial^2 \bar{p}}{\partial y^2} = \bar{\mu}\Lambda \frac{d\bar{h}}{d\theta} \tag{2.2.2}$$

Eq. (2.2.2) is simply the Reynolds equation for an incompressible lubricant.

In one-D approximation, Eq. (2.2.2) reduces to:

$$\frac{d}{d\theta}\left(\bar{h}^3 \frac{d\bar{p}}{d\theta}\right) = \bar{\mu}\Lambda \frac{d\bar{h}}{d\theta} \tag{2.2.3}$$

Integrating Eq. (2.2.3) twice, we have:

$$\bar{p} = \bar{\mu}\Lambda \int_0^\theta \frac{1}{\bar{h}^2} d\theta + C_1 \int_0^\theta \frac{1}{\bar{h}^3} d\theta + C_2 \tag{2.2.4}$$

The appropriate boundary conditions for the one-D problem are:

$$\begin{aligned} &\bar{p} = 1 \qquad at \qquad \theta = 0; \\ &\frac{d\bar{p}}{d\theta} = 0 \quad at \qquad \theta = \theta_{cav} \end{aligned} \tag{2.2.5}$$

where θ_{cav} is the "cavitation" angle where the pressure becomes sub-ambient, or, "negative".

Evaluating the integration constants C_1 and C_2 using Eq. (2.2.4) yields the following expression for pressure:

$$\bar{p} = \bar{\mu}\Lambda\int_0^{\theta}\frac{1}{\bar{h}^2}d\theta - \bar{\mu}\Lambda\bar{h}_{cav}\int_0^{\theta}\frac{1}{\bar{h}^3}d\theta + 1 \tag{2.2.6}$$

where

$$\bar{h}_{cav} = 1 + \varepsilon\cos\theta_{cav} + \alpha(\bar{p}\big|_{\theta=\theta_{cav}} - 1) \tag{2.2.7}$$

is the film thickness at the "cavitation" angle, θ_{cav}.

Applying $\bar{p}\big|_{\theta=\theta_{cav,}} = 1$ to equation (2.2.6) we obtain:

$$\int_0^{\theta_{cav}}\frac{1}{\bar{h}^2}d\theta = (1+\varepsilon\cos\theta_{cav})\int_0^{\theta_{cav}}\frac{1}{\bar{h}^3}d\theta \tag{2.2.8}$$

Eq. (2.2.8) can be solved using the numerical bi-section search method for the "cavitation" angle, θ_{cav}. Because the foil compliance under the action of hydrodynamic pressure affects the film thickness, *h*, and that the lubricant film geometry is not fixed, an iteration scheme that makes use of Eq. (2.1.9) is needed to determine the actual pressure expressed by Eq. (2.2.6).

Since the hydrodynamic pressure at $\Lambda \to 0$ is small and its influence on top foil deformation is negligible, approximation can be made by treating the film geometry as that of rigid bearing. In this case, the integrations $\int_0^{\theta}\frac{1}{\bar{h}^2}d\theta$ and $\int_0^{\theta}\frac{1}{\bar{h}^3}d\theta$ in Eq. (2.2.6) can be evaluated by using Sommerfeld substitution defined as

$$\cos\gamma = \frac{\varepsilon + \cos\theta}{1+\varepsilon\cos\theta} \tag{2.2.9}$$

As a result, the expression for pressure reads:

$$\bar{p} = 1 + \bar{\mu}\Lambda\frac{\cos^{-1}(\frac{\varepsilon+\cos\theta}{1+\varepsilon\cos\theta}) \mp \varepsilon\sqrt{1-(\frac{\varepsilon+\cos\theta}{1+\varepsilon\cos\theta})^2}}{(1-\varepsilon^2)^{3/2}} - \frac{2\bar{\mu}\Lambda(1-\varepsilon^2)}{(2+\varepsilon^2)(1-\varepsilon^2)^{5/2}}$$

$$\times\left[\cos^{-1}\left(\frac{\varepsilon+\cos\theta}{1+\varepsilon\cos\theta}\right)\mp 2\varepsilon\sqrt{1-\left(\frac{\varepsilon+\cos\theta}{1+\varepsilon\cos\theta}\right)^2}+\frac{\varepsilon^2}{2}\cos^{-1}\left(\frac{\varepsilon+\cos\theta}{1+\varepsilon\cos\theta}\right)\right.$$

$$\left.+\frac{\varepsilon^2}{2}\frac{\varepsilon+\cos\theta}{1+\varepsilon\cos\theta}\sqrt{1-\left(\frac{\varepsilon+\cos\theta}{1+\varepsilon\cos\theta}\right)^2}\right] \tag{2.2.10}$$

Case 2: High bearing numbers ($\Lambda\to\infty$)

As bearing speed $\omega\to\infty$ ($\Lambda\to\infty$), $p\to\infty$. For the pressure field to remain bounded as $\Lambda\to\infty$, it is necessary that in Eq. (2.1.11)

$$\frac{\partial}{\partial\theta}\left(\bar{p}\bar{h}\right)\to 0 \tag{2.2.11}$$

implying that $\bar{p}\bar{h}$ is constant and $\bar{p}\propto\frac{1}{\bar{h}}$ (see [9]).

Therefore,

$$\bar{p}=\frac{\widetilde{A}}{1+\varepsilon\cos\theta+\alpha(\bar{p}-1)} \tag{2.2.12}$$

where $\widetilde{A}$ is a constant yet to be determined.

To evaluate $\widetilde{A}$, we note that theoretically the hydrodynamic pressure is nil when the bearing runs concentrically, therefore, at $\varepsilon=0$, $\bar{p}=1$, and from Eq. (2.2.12) we have:

$$\bar{p}=\widetilde{A}=1 \tag{2.2.13}$$

Therefore,

$$\bar{p}=\frac{1}{1+\varepsilon\cos\theta+\alpha(\bar{p}-1)} \tag{2.2.14}$$

Solving Eq. (2.2.14) for $\bar{p}$ yields:

$$\bar{p}=\frac{-(1+\varepsilon\cos\theta-\alpha)+\sqrt{(1+\varepsilon\cos\theta-\alpha)^2+4\alpha}}{2\alpha} \tag{2.2.15}$$

Eq.(2.2.15) can be used to estimate the hydrodynamic pressure that a foil bearing can generate under various operation conditions, i.e., eccentricity ratios. In order to carrying out this estimation, an iteration scheme is required to find the eccentricity ratios of different operation conditions. The procedure begins by evaluating pressure using Eq. (2.2.15) with initial guess of ε that satisfies an arbitrarily given film thickness, and determining the top foil deformation using the resultant pressure. In order to maintain h_{min} of the given film thickness, it is necessary to move the shaft towards the minimum film thickness, namely, modify the eccentricity ratio, by the same amount of the maximum deformation of the top foil, which always occurs at 180° in this case. That is,

$$\varepsilon^{n+1} = \varepsilon^{n} + \Delta\varepsilon^{n+1} \tag{2.2.16}$$

where

$$\Delta\varepsilon^{n+1} = \bar{h}^{n+1}\Big|_{\theta=180} - \bar{h}^{n}\Big|_{\theta=180} \tag{2.2.17}$$

and n is the iteration number. After the new eccentricity ratio is determined, repeating the calculation until two successive iterations fall below a specified tolerance.

By eliminating the "negative" pressure, the converged pressure can be used to estimate the maximum load of the bearing under different operation conditions. One of the ways of eliminating the "negative" pressure is to impose an ambient pressure on the boundaries, followed by equally modifying the pressure at interior nodes by the difference that exists between the boundary solution from the analysis and the actual boundary pressure, i.e.

$$\bar{p} = 1 - \frac{-(1+\varepsilon-\alpha) + \sqrt{(1+\varepsilon-\alpha)^2 + 4\alpha}}{2\alpha} + \frac{-(1+\varepsilon\cos\theta-\alpha) + \sqrt{(1+\varepsilon\cos\theta-\alpha)^2 + 4\alpha}}{2\alpha} \tag{2.2.18}$$

Accordingly, the max pressure can be obtained by differentiate equation (2.2.18) with respect to θ, that is:

$$\overline{p}_{\max} = 1 + \frac{2\varepsilon - \sqrt{(1+\varepsilon-\alpha)^2 + 4\alpha} + \sqrt{(1-\varepsilon-\alpha)^2 + 4\alpha}}{2\alpha} \tag{2.2.19}$$

Using the pressure of one-dimensional problem, Eq. (2.2.18), over the whole bearing length the maximum load-carrying capacity can be estimated as:

$$W_{\max} = p_a LR\sqrt{\left(\int_0^{2\pi} \overline{p}\cos\theta d\theta\right)^2 + \left(\int_0^{2\pi} \overline{p}\sin\theta d\theta\right)^2} \tag{2.2.20}$$

Eq. (2.2.19) and (2.2.20) can be used as an indication of the highest possible pressure a foil bearing can generate and the maximum possible load performance of a foil bearing. The solutions to limiting cases are also useful for verifying the results of numerical solutions that will be carried out in a later stage.

2.3 Thermohydrodynamic Analysis (THD)

The schematic that describes the motion of the lubricant (gas) in a foil bearing is shown in Fig. 6.

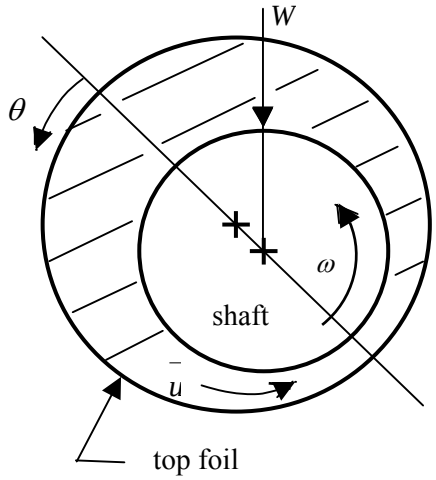

Fig. 6 Schematic of the fluid flow in a foil bearing

In Fig. 6, shaded area is the fluid film. Its outer boundary, the top foil, may not be circular in foil bearing application. In Cartesian coordinate, the velocity $\vec{u}$ has three components as defined in Fig. 7.

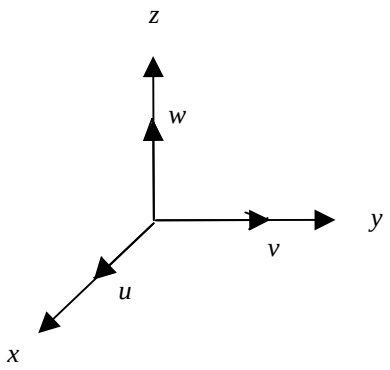

Fig. 7. Velocity components of fluid flow in a foil bearing

The system of equations that is necessary for the steady-state thermohydrodynamic analysis of a compressible fluid are:

$$\rho c_p \vec{u} \cdot \nabla T = k\nabla^2 T + \vec{u} \cdot \nabla p + \Phi$$

$$\frac{1}{R^2}\frac{\partial}{\partial \theta}\left(\frac{ph^3}{\mu T}\frac{\partial p}{\partial \theta}\right) + \frac{\partial}{\partial y}\left(\frac{ph^3}{\mu T}\frac{\partial p}{\partial y}\right) = 6\omega \frac{\partial}{\partial \theta}\left(\frac{ph}{T}\right) \tag{2.3.1}$$

where

$$\Phi = \mu\left[2\left(\frac{\partial u}{\partial x}\right)^2 + 2\left(\frac{\partial v}{\partial y}\right)^2 + 2\left(\frac{\partial w}{\partial z}\right)^2 + \left(\frac{\partial u}{\partial y} + \frac{\partial v}{\partial x}\right)^2 + \left(\frac{\partial v}{\partial z} + \frac{\partial w}{\partial y}\right)^2 + \left(\frac{\partial w}{\partial x} + \frac{\partial u}{\partial z}\right)^2\right] \tag{2.3.2}$$

represents the viscous dissipation, $\vec{u}$ is the velocity vector including three components: u is the linear velocity of gas flow in the direction of motion, v is the linear velocity of gas flow in axial direction, and w is the linear velocity of gas flow across the film.

The temperature gradient in the axial direction, $\frac{\partial T}{\partial y}$, is shown by Dowson et al. [10] to be small; hence the heat conduction term, $k\frac{\partial^2 T}{\partial y^2}$, is considered to be negligible. Further, an analysis done by Khonsari et. al [11] have shown that heat conduction along the circumference, $\frac{\partial^2 T}{\partial x^2}$, is negligible. When compared to the velocity gradients $\frac{\partial u}{\partial z}$ and $\frac{\partial v}{\partial z}$, all the other velocity gradients in Eq. (2.3.2) are relatively small and can be neglected. Furthermore, the pressure gradient across the film is nil according to Dowson [12]. Hence, the energy equation in Eq. (2.3.1) reduces to:

$$\rho c_p\left(u\frac{\partial T}{\partial x}+w\frac{\partial T}{\partial z}\right)=k\frac{\partial^2 T}{\partial z^2}+u\frac{\partial p}{\partial x}+v\frac{\partial p}{\partial y}+\mu\left[\left(\frac{\partial u}{\partial z}\right)^2+\left(\frac{\partial v}{\partial z}\right)^2\right] \qquad (2.3.3)$$

At the bearing mid-plane, y = 0 and $\frac{\partial p}{\partial y}=0$, and that $v=\frac{1}{2\mu}\frac{\partial p}{\partial y}(z^2-zh)=0$. Therefore, Eq. (2.3.3) reduces to:

$$\rho c_p\left(u\frac{\partial T}{\partial x}+w\frac{\partial T}{\partial z}\right)=k\frac{\partial^2 T}{\partial z^2}+u\frac{dp_\theta}{dx}+\mu\left(\frac{\partial u}{\partial z}\right)^2 \qquad \text{at} \quad y = 0 \qquad (2.3.4)$$

where $\overline{p}_\theta$ is the pressure of the bearing mid-plane from the solution of two-D Reynolds' equation.

The viscosity-temperature relationship is given by Salehi et al. [13]:

$$\mu = a(T - T_{ref}) \qquad (2.3.5)$$

where $a = 4\times10^{-8}$ and $T_{ref} = -458.75$ when T is in °C.

Let $\tau = T - T_{ref}$, we have

$$\mu = a\tau \qquad (2.3.6)$$

and

$$\rho c_p u \frac{\partial \tau}{\partial x} = k \frac{\partial^2 \tau}{\partial z^2} + u \frac{dp_\theta}{dx} + a\tau \left(\frac{\partial u}{\partial z} \right)^2 \tag{2.3.7}$$

In dimensionless form, equation (2.3.7) reads:

$$\begin{aligned} \overline{\rho} \left(\overline{u} \frac{\partial \overline{T}}{\partial \theta} + \frac{1}{\overline{h}} \overline{w} \frac{\partial \overline{T}}{\partial \overline{z}} \right) = \frac{\lambda_2}{\lambda_1} \frac{1}{\overline{h}^2} \frac{\partial^2 \overline{T}}{\partial \overline{z}^2} + \overline{u} \frac{\lambda_3}{\lambda_1} \frac{d\overline{p}_\theta}{d\theta} \\ + \frac{\lambda_4}{\lambda_1} \frac{\overline{T}}{\overline{h}^2} (\frac{\partial \overline{u}}{\partial \overline{z}})^2 + \frac{\lambda_4}{\lambda_1} \frac{1}{\overline{h}^2} (\frac{\partial \overline{u}}{\partial \overline{z}})^2 \end{aligned} \tag{2.3.8}$$

where

$$\overline{\rho} = \frac{\rho}{\rho_0},\ \overline{u} = \frac{u}{U},\ \overline{w} = \left(\frac{R}{C} \right) \frac{w}{U},$$

$$\overline{p} = \frac{p}{p_a},\ \overline{h} = \frac{h}{C},\ \overline{z} = \frac{z}{h},\ \overline{T} = \frac{\tau - \tau_0}{\tau_0},$$

$$\tau_0 = T_0 - T_{ref};\ \lambda_1 = \frac{\rho_0 c_p RU}{k};\ \lambda_2 = (\frac{R}{C})^2; \tag{2.3.9}$$

$$\lambda_3 = \frac{p_a RU}{k\tau_0};\ \lambda_4 = (\frac{R}{C})^2 \frac{aU^2}{k}$$

Letting

$$\kappa_1 = \frac{\lambda_4}{\lambda_1} = \frac{aRU}{\rho_0 c_p C^2},$$

$$\kappa_2 = \sqrt{\frac{\lambda_4}{\lambda_2}} = U\sqrt{a/k}, \tag{2.3.10}$$

$$\kappa_3 = \frac{\lambda_3}{\lambda_1} = \frac{p_a}{\rho_0 c_p \tau_0}$$

Eq. (2.3.6) becomes:

$$\overline{\rho}\left(\overline{u}\frac{\partial\overline{T}}{\partial\theta}+\frac{1}{\overline{h}}\overline{w}\frac{\partial\overline{T}}{\partial\overline{z}}\right)=\frac{\kappa_1}{\kappa_2^2}\frac{1}{\overline{h}^2}\frac{\partial^2\overline{T}}{\partial\overline{z}^2}+\overline{u}\kappa_3\frac{d\overline{p}_\theta}{d\theta}+\kappa_1\frac{\overline{T}}{\overline{h}^2}\left(\frac{\partial\overline{u}}{\partial\overline{z}}\right)^2+\kappa_1\frac{1}{\overline{h}^2}\left(\frac{\partial\overline{u}}{\partial\overline{z}}\right)^2 \tag{2.3.11}$$

The velocity profile in the direction of motion is given by:

$$u=\frac{z}{h}U+\frac{1}{2\mu}\frac{dp}{dx}(z^2-zh)\quad\text{or}\quad\overline{u}=\overline{z}+\kappa_4\overline{h}^2(\overline{z}^2-\overline{z})\frac{d\overline{p}}{d\overline{x}} \tag{2.3.12}$$

where $\kappa_4=\dfrac{p_0C^2}{2\mu RU}$.

At the bearing mid-plane, $v = 0$, and the continuity equation is expressed as:

$$\frac{\partial u}{\partial x}+\frac{\partial w}{\partial z}=0\qquad\text{or}\qquad\frac{\partial\overline{u}}{\partial\theta}+\frac{\partial\overline{w}}{\overline{h}\partial\overline{z}}=0 \tag{2.3.13}$$

therefore,

$$\overline{w}=-\overline{h}\int_0^{\overline{z}}\frac{\partial\overline{u}}{\partial\overline{x}}\partial\overline{z}=-\kappa_4\left(2\overline{h}^2\frac{d\overline{h}}{d\overline{x}}\frac{d\overline{p}}{d\overline{x}}+\overline{h}^3\frac{d^2\overline{p}}{d\overline{x}^2}\right)\left(\frac{\overline{z}^3}{3}-\frac{\overline{z}^2}{2}\right) \tag{2.3.14}$$

The appropriate boundary conditions are derived in Appendix A with the results:

$$\overline{T}(0,\overline{z})=\overline{T}_i(\overline{z})$$

$$\overline{T}(\overline{x},1)=\overline{T}_s \tag{2.3.15}$$

$$\left(\overline{T}+\gamma\frac{\partial\overline{T}}{\partial\overline{z}}\right)_{\overline{z}=0}=0$$

where

$$\gamma(\theta)=-\left[1+\frac{1}{\overline{h}(\theta)}\left(\frac{R}{C}\right)\right]\left[\frac{1}{\aleph(\theta)}+\frac{k}{k_B}\ln\left(1+\frac{t_B}{R+C\overline{h}(\theta)}\right)\right] \tag{2.3.16}$$

where

$$\aleph(\theta) = \frac{h_{conv}\left(R + C\,\bar{h}(\theta) + t_B\right)}{k} \tag{2.3.17}$$

The parameter $\bar{T}_i$ in Eq. (2.3.15) represent the dimensionless temperature at $\theta = 0$, i.e. the "inlet" temperature. Since the re-circulating gas temperature is generally greater than that of the fresh gas entering the bearing at the ambient temperature, a mixing temperature must be calculated. The mixing temperature represents the effective temperature after the warm gas mixes with the fresh gas. A simple schematic of the control volume representing the region where the air mixes is shown in Fig. 8.

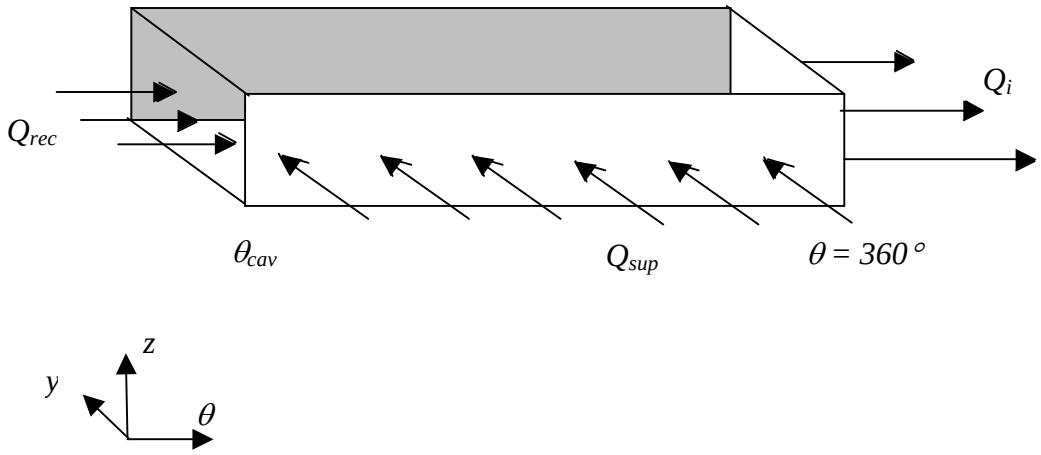

Fig. 8 Schematic of the region where re-circulate air mixes with fresh air (shaded plane is the symmetric mid-plane)

An energy balance in this control volume is given by Khonsari et. al [14]:

$$\bar{T}_i = \frac{\bar{T}_{rec}\bar{Q}_{rec} + \bar{T}_{\sup}\bar{Q}_{\sup}}{\bar{Q}_{rec} + \bar{Q}_{\sup}} \tag{2.3.18}$$

where $\bar{Q}_{\sup}$ is the dimensionless incoming flow rate which shall be the same amount as the leakage flow rate, $\bar{Q}_{leak}$. Since the "negative" pressure occurs at different locations for

different y planes along the bearing length, the leakage flow rate, $\overline{Q}_{leak}$, and re-circulated flow rate, $\overline{Q}_{rec}$, are calculated using integration method:

$$Q_{leak} = 2\int_0^{\theta_{cav}} \left(R\int_0^h v\Big|_{y=\frac{L}{2}} dz \right) d\theta = 2\int_0^{\theta_{cav}} R\left(-\frac{h^3}{12\mu}\frac{\partial p}{\partial y}\bigg|_{y=\frac{L}{2}} \right) d\theta \tag{2.3.19}$$

or

$$\overline{Q}_{leak} = -2\int_0^{\theta_{cav}} \frac{\overline{h}^3}{12\overline{\mu}}\frac{\partial \overline{p}}{\partial \overline{y}}\bigg|_{\overline{y}=0} d\theta \tag{2.3.20}$$

and

$$\begin{aligned} Q_{rec} &= 2\int_0^{\frac{L}{2}}\int_0^{h_{cav}} u\Big|_{\theta=\theta_{cav}} dzdy = 2\int_0^{\frac{L}{2}} \left(\frac{h_{cav}U}{2} - \frac{h_{cav}^3}{12\mu}\frac{\partial p}{R\partial\theta}\bigg|_{\theta=\theta_{cav}} \right) dy \\ &= U\int_0^{\frac{L}{2}} h_{cav}dy + 2\int_0^{\frac{L}{2}} -\frac{h_{cav}^3}{12\mu}\frac{\partial p}{R\partial\theta}\bigg|_{\theta=\theta_{cav}} dy \end{aligned} \tag{2.3.21}$$

or

$$\overline{Q}_{rec} = \frac{\mu_0 UL^2}{4p_a RC^2}\int_0^1 \overline{h}_{cav}d\overline{y} - \frac{1}{6\overline{\mu}_{cav}}\left(\frac{L}{D}\right)^2 \int_0^1 \overline{h}_{cav}^3 \frac{\partial \overline{p}}{\partial\theta}\bigg|_{\theta=\theta_{cav}} d\overline{y} \tag{2.3.22}$$

where $\overline{Q}_{leak} = \dfrac{Q_{leak}}{Q_{ref}}$ and $Q_{ref} = \dfrac{2p_a RC^3}{\mu_0 L}$.

The dimensionless $\overline{T}_s$ in Eq. (2.3.15) is the dimensionless shaft temperature. Since the shaft is generally rotating at high speed, it is appropriate to assume that $\overline{T}_s$ is constant and to be determined by imposing the following energy balance [15]:

$$\int_0^{2\pi} k\frac{\partial \overline{T}}{\partial \overline{z}}\bigg|_{\overline{z}=1} d\theta = 0 \tag{2.3.23}$$

This boundary condition describes that the net heat flux into the shaft equals to zero. In a journal type bearing, temperature of the fluid film builds up in the convergent region and cools down in the divergent region. Therefore, along the bearing circumference heat goes into shaft from the fluid film in the high temperature region of the film and a reverse process occurs in the relatively low temperature region. For an insulated bushing, the net heat flux into the shaft equals to zero. In the foil bearing application, the top foil is very thin and it is separated from the sleeve by narrow contacts with the bump foil. Therefore, the heat conduction from the fluid film through bushing is somewhat restricted. In this case, the assumption of net flux into the shaft can still be assumed valid.

To estimate h_{conv} in Eq. (2.3.17), one needs to find the Nusselt number, N_u, of the convective fluid applied to the top foil bottom surface. In functional form,

$$h_{conv} = \frac{k_{conv} N_u}{D_h} \tag{2.3.24}$$

where D_h is the hydrodynamic length of the convective fluid.

Based on the results of C. L. Hwang, the mean Nusselt number can be found empirically through Gratz number defined as:

$$G_z = \frac{L \diagup D_h}{R_e P_r} \tag{2.3.25}$$

where P_r is the Prandtl number and R_e is the Reynolds' number of the convective fluid.

CHAPTER3. NUMERICAL PROCEDURES

3.1 Numerical Algorithm for Compressible Reynolds' Equation

Treatment of the Reynolds' equation (2.1.11) in section 2.1 requires an iterative numerical scheme. The procedure begins by expanding Eq. (2.1.11) as follows:

$$\begin{aligned}&\frac{\partial^2 \overline{p}}{\partial \theta^2}+\left(\frac{D}{L}\right)^2 \frac{\partial^2 \overline{p}}{\partial \overline{y}^2} \\ &=-\frac{1}{\overline{p}}\left[(\frac{\partial \overline{p}}{\partial \theta})^2+\left(\frac{D}{L}\right)^2(\frac{d\partial \overline{p}}{\partial \overline{y}})^2\right]-\frac{3}{\overline{h}}\frac{\partial \overline{h}}{\partial \theta}\frac{\partial \overline{p}}{\partial \theta}+\frac{\overline{\mu}\Lambda}{\overline{p}\overline{h}^2}\frac{\partial \overline{p}}{\partial \theta}+\frac{\overline{\mu}\Lambda}{\overline{h}^3}\frac{\partial \overline{h}}{\partial \theta}\end{aligned} \tag{3.1.1}$$

Eq. (3.1.1) has a similar form of Poisson's equation except that the RHS of the equation is a nonlinear function of the hydrodynamic pressure. A standard Poisson's equation can be solved using the Liebmann method or the successive over-relaxation (the so-called "SOR") [16] for a faster convergence. The finite difference approximation of the left hand side (LHS) and the right hand side (RHS) of Eq. (3.1.1) are:

$$LHS=\frac{\overline{p}_{i+1,j}-2\overline{p}_{i,j}+\overline{p}_{i-1,j}}{(\Delta\theta)^2}+\left(\frac{D}{L}\right)^2\frac{\overline{p}_{i,j+1}-2\overline{p}_{i,j}+\overline{p}_{i,j-1}}{(\Delta y)^2} \tag{3.1.2}$$

and

$$\begin{aligned}RHS=&-\frac{1}{\overline{p}_{i,j}}\left[\left(\frac{\partial \overline{p}}{\partial \theta}\bigg|_i\right)^2+\left(\frac{D}{L}\right)^2\left(\frac{\partial \overline{p}}{\partial \overline{y}}\bigg|_j\right)^2\right]-\left(\frac{3}{\overline{h}_{i,j}}\frac{d\overline{h}}{d\theta}\bigg|_i-\frac{\overline{\mu}\Lambda}{\overline{p}_{i,j}\overline{h}_{i,j}^{\,2}}\right)\frac{d\overline{p}}{d\theta}\bigg|_i \\ &+\frac{\overline{\mu}\Lambda}{\overline{h}_{i,j}^3}\frac{d\overline{h}}{d\theta}\bigg|_i\end{aligned} \tag{3.1.3}$$

The solution begins by evaluating the RHS using the initial guesses on pressure, $\overline{p}_{i,j}$, and film thickness, $\overline{h}_{i,j}$, and solving Eq. (3.1.1) for pressure and repeating the calculation until convergence is achieved for a given film thickness. Convergence is assumed when

the relative error between two successive iterations falls below a specified tolerance value. For low bearing numbers, or the bearing speed is less than 20,000 rpm, 50 finite difference grid points along circumferential direction and 10 grids along axial direction over half of the bearing length was found to be sufficient to achieve convergence with a tolerance value of 0.1%. However, for high bearing numbers, finer meshes such as 100 by 20 and more stringent tolerance value, say 0.001%, were necessary with considerably greater computational time due to the high nonlinearity of the problem.

Once the pressure converges for a given gas film geometry, another iteration scheme is employed to seek the actual film geometry as the result of dynamic interaction between hydrodynamic pressure and foil compliance. In a foil bearing application, there are two factors that determine the actual film geometry: one is the deformation of the top foil and the other is the location of the shaft. The numerical procedure adapted for tracking the movement of the shaft is to modify the eccentricity ratio in Eq. (2.1.9) iteratively as shown below.

$$\varepsilon^{n+1} = \varepsilon^{n} + \Delta\varepsilon^{n+1} \tag{3.1.4}$$

where

$$\Delta\varepsilon^{n+1} = \bar{h}_{\min}^{n+1} - \bar{h}_{\min}^{n} \tag{3.1.5}$$

and n is the iteration number. This procedure assures that a positive h_{min} is maintained in the process of seeking the final solution of pressure. In this fashion, h_{min} can be treated as a controllable parameter in simulation. As we shall discuss in section 4, this is necessary in order to simulate the experimental results reported in [4]. Convergence is assumed when the relative error between two successive iterations falls below a tolerance value of 0.1%. Under-relaxation of pressure effect on the deformation of top foil and the change in

eccentricity ratio between successive iterations was necessary when needed to achieve the convergence. Under-relaxation between successive iterations is given by the formula:

$$\bar{h}^{n+1} = \varsigma \bar{h}^{n+1} + (1-\varsigma)\bar{h}^{n} \tag{3.1.6}$$

where ς is the under-relaxation parameter and n is the iteration number. ς equal to 0.1 to 0.3 are typically used.

After the pressure and the lubricant film profile are simultaneously determined, numerical integration is used for the load-carrying capacity calculation. Both Simpson's 1/3 rule and 3/8 rules are used as the numerical integration method.

3.2 Numerical Algorithm for Energy Equation

To solve Eq. (2.3.11) in section 2.3, a transformation operator given by Ezzat and Rhode [15]:

$$\begin{aligned} \frac{\partial}{\partial\theta} &= \frac{\partial}{\partial\bar{x}} - \frac{\partial\bar{h}}{\partial\bar{x}}\frac{\bar{z}}{\bar{h}}\frac{\partial}{\partial\bar{z}} \\ \frac{d}{d\theta} &= \frac{d}{d\bar{x}} \end{aligned} \tag{3.2.1}$$

is used so that the following equation over a computational domain emerges:

$$\begin{aligned} &\bar{\rho}\left[\bar{u}\frac{\partial\bar{T}}{\partial\bar{x}} + \frac{1}{\bar{h}}\left(\bar{w} - \bar{u}\bar{z}\frac{\partial\bar{h}}{\partial\bar{x}}\right)\frac{\partial\bar{T}}{\partial\bar{z}}\right] \\ &= \frac{\kappa_1}{\kappa_2^2}\frac{1}{\bar{h}^2}\frac{\partial^2\bar{T}}{\partial\bar{z}^2} + \kappa_3\bar{u}\frac{d\bar{p}_\theta}{d\bar{x}} + \kappa_1\frac{\bar{T}}{\bar{h}^2}\left(\frac{\partial\bar{u}}{\partial\bar{z}}\right)^2 + \kappa_1\frac{1}{\bar{h}^2}\left(\frac{\partial\bar{u}}{\partial\bar{z}}\right)^2 \end{aligned} \tag{3.2.2}$$

With Eq. (3.2.2), Eq. (2.3.12) and (2.3.14) from sections 2.3, a numerical marching technique is developed to obtain the temperature field. Using central-difference approximation along z and backward-difference along x, Eq. (3.2.2) is written:

$$\overline{\rho}_j\left(\overline{u}_{i,j}\frac{\overline{T}_{i,j}-\overline{T}_{i,j-1}}{\Delta\overline{x}}+\frac{1}{\overline{h}_j}\left(\overline{w}_{i,j}-\overline{u}_{i,j}\overline{z}_i\frac{d\overline{h}}{d\overline{x}}\bigg|_{\overline{x}_j}\right)\frac{\overline{T}_{i+1,j}-\overline{T}_{i-1,j}}{2\Delta\overline{z}}\right)$$

$$=\frac{\kappa_1}{{\kappa_2}^2}\frac{1}{\overline{h}_j^2}\frac{\overline{T}_{i+1,j}-2\overline{T}_{i,j}+\overline{T}_{i-1,j}}{\left(\Delta\overline{z}\right)^2}+\kappa_3\overline{u}_{i,j}\frac{d\overline{p}}{d\overline{x}}\bigg|_{\overline{x}_j}+\kappa_1\frac{\overline{T}_{i,j}}{\overline{h}_j^2}\left(\frac{\partial\overline{u}}{\partial\overline{z}}\bigg|_{i,j}\right)^{2^2}$$

$$+\kappa_1\frac{1}{\overline{h}_j^2}\left(\frac{\partial\overline{u}}{\partial\overline{z}}\bigg|_{i,j}\right) \tag{3.2.3}$$

Re-arranging yields:

$$\vec{a}\overline{T}_{i-1,j}+\vec{b}\overline{T}_{i,j}+\vec{c}\overline{T}_{i+1,j}=\vec{d}\overline{T}_{i,j-1}+\kappa_3\overline{u}_{i,j}\frac{d\overline{p}}{d\overline{x}}\bigg|_{\overline{x}_j}+\kappa_1\frac{1}{\overline{h}_j^2}\left(\frac{\partial\overline{u}}{\partial\overline{z}}\bigg|_{i,j}\right)^2 \tag{3.2.4}$$

where

$$\vec{a}=-\left[\frac{\kappa_1}{{\kappa_2}^2}\frac{1}{\overline{h}_j^2\left(\Delta\overline{z}\right)^2}+\frac{\overline{\rho}_j}{\overline{h}_j 2\Delta\overline{z}}\left(\overline{w}_{i,j}-\overline{z}_i\overline{u}_{i,j}\frac{d\overline{h}}{d\overline{x}}\bigg|_{\overline{x}_j}\right)\right]$$

$$\vec{b}=2\frac{\kappa_1}{{\kappa_2}^2}\frac{1}{\overline{h}_j^2\left(\Delta\overline{z}\right)^2}-\frac{\kappa_1}{\overline{h}_j^2}\left(\frac{\partial\overline{u}}{\partial\overline{z}}\bigg|_{i,j}\right)^2+\frac{1}{\Delta\overline{x}}\overline{\rho}_j\overline{u}_{i,j} \tag{3.2.5}$$

$$\vec{c}=-\left[\frac{\kappa_1}{{\kappa_2}^2}\frac{1}{\overline{h}_j^2\left(\Delta\overline{z}\right)^2}-\frac{\overline{\rho}_j}{\overline{h}_j 2\Delta\overline{z}}\left(\overline{w}_{i,j}-\overline{z}_i\overline{u}_{i,j}\frac{d\overline{h}}{d\overline{x}}\bigg|_{\overline{x}_j}\right)\right]$$

$$\vec{d}=\frac{1}{\Delta\overline{x}}\overline{\rho}_j\overline{u}_{i,j}$$

Eq. (3.2.4) is to be applied at every point where $\overline{T}$ is unknown, including the points at the boundaries as well as the interior points.

To implement the derivative boundary condition at the lubricant-bushing interface, we use the concept of fictitious nodes. Letting z_L be fictitious points to the left of z = 0, we have

$$\vec{a}\overline{T}_{L,j} + \vec{b}\overline{T}_{1,j} + \vec{c}\overline{T}_{2,j} = \vec{d}\overline{T}_{1,j-1} + \kappa_3 \overline{u}_{i,j} \left.\frac{d\overline{p}}{d\overline{x}}\right|_{\overline{x}_j} + \kappa_1 \frac{1}{\overline{h}_j^2}\left(\left.\frac{\partial \overline{u}}{\partial \overline{z}}\right|_{i,j}\right)^2 \tag{3.2.6}$$

Applying the central-difference operator to the derivative boundary condition in Eq. (2.3.15) yields:

$$\gamma \frac{\overline{T}_{2,j} - \overline{T}_{L,j}}{2\Delta\overline{z}} = -\overline{T}_{1,j} \tag{3.2.7}$$

Eliminating the fictitious points by solving Eq. (3.2.7) for $\overline{T}_L$, we have,

$$\overline{T}_{L,j} = \frac{2\Delta\overline{z}}{\gamma}\overline{T}_{1,j} + \overline{T}_{2,j} \tag{3.2.8}$$

Combining Eq. (3.2.8) and (3.2.6) yields,

$$\begin{aligned} &\left(\frac{2\vec{a}(1)\Delta\overline{z}}{\gamma(j)} + \vec{b}(1)\right)\overline{T}_{1,j} + \left(\vec{a}(1) + \vec{c}(1)\right)\overline{T}_{2,j} \\ &= \vec{d}(1)\overline{T}_{1,j-1} + \kappa_3 \overline{u}_{i,j} \left.\frac{d\overline{p}}{d\overline{x}}\right|_{\overline{x}_j} + \kappa_1 \frac{1}{\overline{h}_j^2}\left(\left.\frac{\partial \overline{u}}{\partial \overline{z}}\right|_{i,j}\right)^2 \end{aligned} \tag{3.2.9}$$

as the first equation of Eq. (3.2.6), while the rest of Eq.(3.2.6) remain the same. Eq. (3.2.6) is now ready to be solved.

According to section 2.3, the other two boundaries for marching the temperature field is not prescribed and that we have to resort to numerical techniques to determine them. The solution begins with solving the temperature field subject to a given inlet temperature and shaft temperature using marching technique. After obtaining this temperature distribution a heat balance is performed over the region where the air mixes, "negative" pressure region, and Eq. (3.2.18) is used to determine the inlet temperature in an iteration scheme. Convergence is assumed when two successive iterations fall below a specified tolerance value, 0.1%. Once the temperature converges for a mixed inlet

temperature, the net heat flux from the fluid film into shaft is calculated using the Fourier Law. According to Eq. (2.3.23), the net heat flux into the shaft must be nil. The bisection search method is used for this purpose to determine the final temperature field.

Note that the density, ρ, is a function of both pressure and temperature and can be expressed as:

$$\rho(\theta,z)\big|_{y=0} = \rho_0 \frac{p_\theta}{p_a}\frac{T_0}{T(\theta,z)}$$

or (3.2.10)

$$\overline{\rho} = \frac{\overline{p}_\theta}{1+(1-K/T_0)\overline{T}}$$

This relation is taken into consideration in the process of marching of temperature.

Once the energy equation is solved based on the knowledge of pressure from isothermal Reynolds' equation, the viscosity is updated using

$$\mu = a\tau$$

or (3.2.11)

$$\overline{\mu} = \frac{a\tau_0}{\mu_0}(1+\overline{T})$$

Then the Reynolds' equation in Eq.(2.3.1) can be solved to incorporate the thermal effects on the hydrodynamic pressure. Corresponding to the dimensionless form of Reynolds' equation in Eq. (2.3.1), we have:

$$\begin{aligned}\frac{\partial^2\overline{p}}{\partial\theta^2}+\left(\frac{D}{L}\right)^2\frac{\partial^2\overline{p}}{\partial z^2} = &-\frac{1}{\overline{p}}\left[(\frac{\partial\overline{p}}{\partial z})^2+\left(\frac{D}{L}\right)^2(\frac{\partial\overline{p}}{\partial\theta})^2\right]\\ &-\left(3\frac{1}{\overline{h}}\frac{d\overline{h}}{d\theta}-\frac{\overline{\mu}\Lambda}{\overline{p}\overline{h}^2}-\frac{1}{\overline{\mu}}\frac{d\overline{\mu}}{d\theta}-\frac{1}{\overline{T}}\frac{d\overline{T}}{d\theta}\right)\frac{\partial\overline{p}}{\partial\theta}\\ &+\frac{\overline{\mu}\Lambda}{\overline{h}^3}\frac{d\overline{h}}{d\theta}-\overline{\mu}\Lambda\frac{1}{\overline{h}^2}\frac{1}{\overline{T}}\frac{d\overline{T}}{d\theta}\end{aligned} \quad (3.2.12)$$

Eq. (3.2.12) can be solved in the same manner as Eq. (3.1.1), except that *RHS* in Eq. (3.1.3) changes to include the thermal effect on hydrodynamic pressure as follows:

$$RHS = -\frac{1}{\overline{p}_{i,j}}\left[\left(\left.\frac{\partial \overline{p}}{\partial \theta}\right|_i\right)^2 + \left(\frac{D}{L}\right)^2\left(\left.\frac{\partial \overline{p}}{d\overline{y}}\right|_j\right)^2\right] - \left(\frac{3}{\overline{h}_{i,j}}\left.\frac{d\overline{h}}{d\theta}\right|_i - \frac{\overline{\mu}\Lambda}{\overline{p}_{i,j}\overline{h}_{i,j}^{\,2}}\right.$$
$$\left. - \frac{1}{\overline{\mu}_j}\left.\frac{d\overline{\mu}}{d\theta}\right|_j - \frac{1}{\overline{T}_j}\left.\frac{d\overline{T}}{d\theta}\right|_j\right)\left.\frac{\partial \overline{p}}{\partial \theta}\right|_i + \frac{\overline{\mu}\Lambda}{\overline{h}_{i,j}^3}\left.\frac{d\overline{h}}{d\theta}\right|_i - \overline{\mu}_j\Lambda\frac{1}{\overline{h}_{i,j}^2}\frac{1}{\overline{T}_j}\left.\frac{d\overline{T}}{d\theta}\right| \tag{3.2.13}$$

Now Eq. (3.2.6) and (3.2.13) have to be solved simultaneously by iterations to reach the steady-state solutions for both pressure and temperature, as described in the flow chart in section 2.

CHAPTER4. LOAD PERFORMANCE AND OPERATIONAL STABILITY FROM ISOTHERMAL HYDRODYNAMIC ANALYSIS

4.1 Numerical Prediction on Maximum Load-carrying Capacity

We seek to verify the isothermal theory using the existing experimental data. Because of the inherently low air viscosity, one of the most important parameters of the gas bearings is their load performance. A number of experiments have been carrying out to test the maximum load-carrying capacity of every generation of foil bearings. The data of one of the tested first generation foil bearings is tabulated in Table 1. The lubricant data are listed in Table 2.

Table 1 Data of a foil bearing 1 (1st generation)

Shaft radius (R)	19.05×10^{-3} m
Bearing length (L)	38.1×10^{-3} m
Bearing clearance (C)	50×10^{-6} m
Top foil thickness (t_B)	0.1016×10^{-3} m
Bump foil thickness (t_{BF})	0.1016×10^{-3} m
Bump pitch (s)	4.572×10^{-3} m
Bump length ($2l$)	3.556×10^{-3} m

Table 2 Lubricant (air) data

Viscosity of lubricant (μ)	184.6×10^{-7} N.s/m^2
Lubricant density (ρ_0)	1.1614 kg/m^3
Specific heat of lubricant (c_p)	1007 J/kg.K
Conductivity of lubricant (k)	26.3×10^{-3} W/k·m

In order to determine the maximum load-carrying capacity numerically, in accordance to the foil experimental procedure reported in [4], the eccentricity ratio shall be pushed to the greatest possible value, while maintaining a positive minimum film thickness for stable operation. In a foil bearing application, the shaft can move towards h_{min} with additional room generated by the deformation of top foil under hydrodynamic pressure. As pointed out in section 2.1, the eccentricity ratio can actually assume a value greater than unity. This proved to be an important consideration in the foil bearing simulations presented in this section. A typical surface profile of a foil bearing in operation compared with that of a rigid bearing is schematically shown in Fig. 9. Also shown is the difference between the eccentricity of a rigid bearing, e_r, and that of a foil bearing, e_f. Under the same load and operating conditions, $e_f > e_r$.

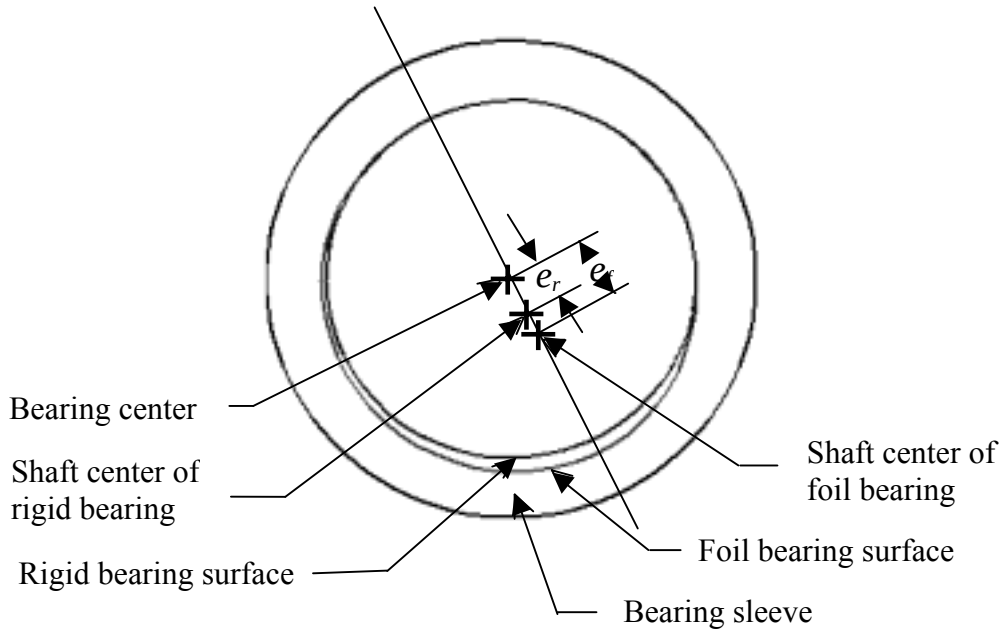

Fig. 9 Schematic of the operational surface profile and eccentricity of a foil bearing compared with a rigid bearing

Experimentally, as documented in [1,4,10], the maximum load was established by gradually increasing the load application at a fixed rotor speed until the observation of sharp rise in bearing torque or temperature, as measured by the sensor imbedded beneath the bearing surface. As an example, the maximum experimental load obtained when running a foil bearing, whose data is tabulated in Table 1, at 45,000 rpm was found to be 230N. The predicted h_{min} of gas film thickness for this case converged at about 11μm at an eccentricity ratio of 1.22. The value of h_{min} corresponds to the smallest gas film which allows the shaft to run stably and that if exceeded could result in bearing instability and that surface-to-surface contact that leads to failure. Shown in Fig. 10 is a 3-D plot of the pressure of the foil bearing. Note that the plot is reversed in θ direction in order to show the sub-ambient pressure, which occurs in the divergent region of the foil bearing. The existence of sub-ambient region provides the suction necessary to replenish the air "pumped out" by side leakage.

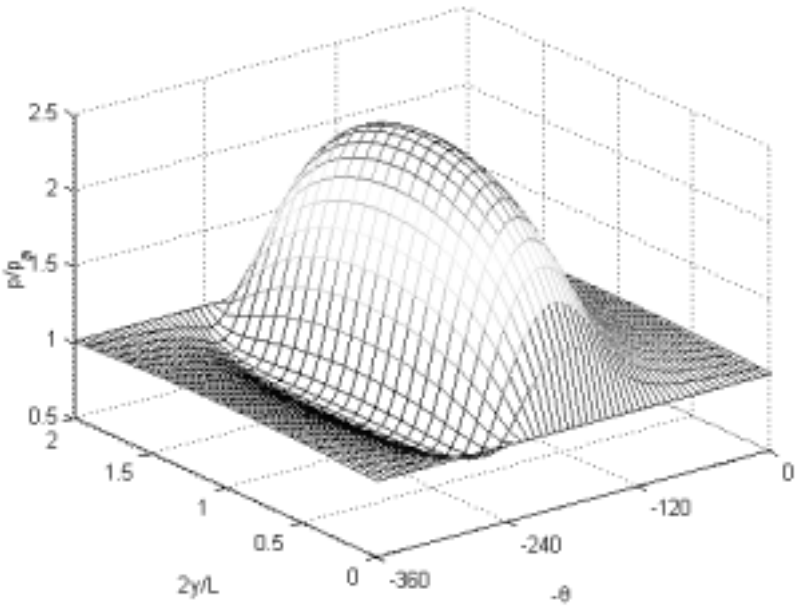

Fig. 10 Hydrodynamic pressure in a foil bearing at 45,000 rpm under 230N.

The results of the prediction of the maximum load-carrying capacity of a first generation foil bearing as a function of the compressibility number is shown in Figure 10. Also shown in that figure are the experimental results reported in [17]. The minimum film thickness assumed for the entire range of operating speeds was h_{min} = 11μm. Clearly, the predicted load-carrying capacity curve is in good agreement with the experimental results over a wide range of speeds simulated.

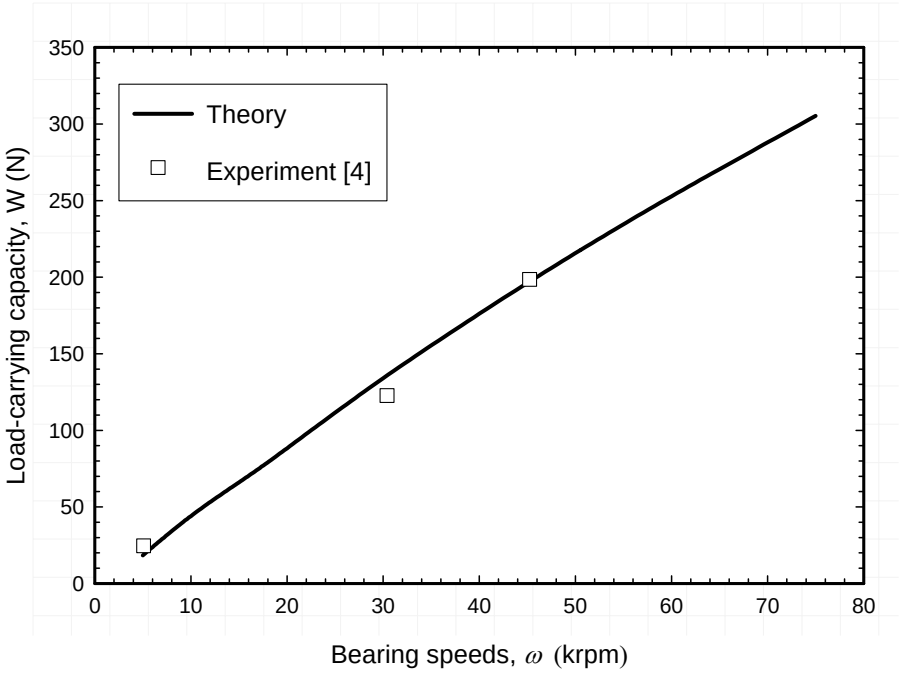

Fig. 11 Simulated load performance compared with experimental data

4.2 Characterization of Fluid-film Geometry, Pressure Distribution, and Operational Stability

Information about the lubricant film geometry is important in order to understand the characteristic of bearing performance. The optimum film profile is one which would provide the highest load-carrying capacity. Shown in Fig. 12 is the film geometry for the bearing running at 30,000 rpm with assumed h_{min} of about 11μm. The corresponding film thickness for a rigid bearing is also plotted for comparison. As revealed in Fig. 12, the

steady-state eccentricity ratio of the foil bearing converged to 1.12 in this case and because of this the fluid film of a foil bearing is more convergent than that of a rigid bearing due to the larger eccentricity ratio.

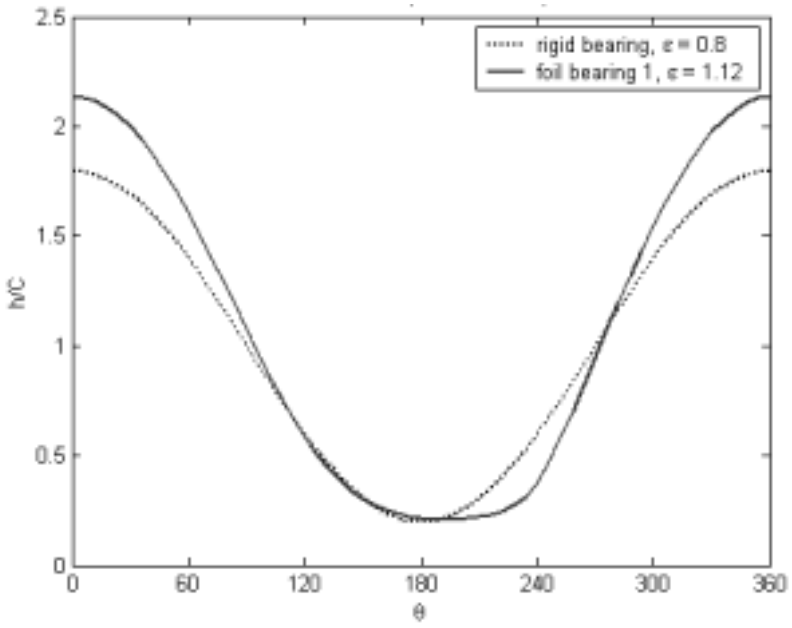

Fig. 12 Converged fluid film geometry (operating speed = 30,000 rpm, h_{min} =11 μm)

Also shown in Fig. 12 is that the foil bearing provides a more uniform profile in the vicinity of h_{min} than does the rigid bearing. Further noticed is that in a foil bearing the convergent region of the film gap spans over a greater area than that of a rigid bearing due to the deformation of the foils under the hydrodynamic pressure.

Fig.13 presents the comparison of the hydrodynamic pressure between a foil bearing and a same sized rigid bearing under the same assumption on h_{min} at 30,000 rpm. Note that in a foil bearing the pressure is spread over a greater area. This leads to a greater load-carrying capacity than its rigid bearing counterpart as shown in Fig. 14. The advantage of load performance of foil bearing over rigid bearing is essentially created by the top foil deformation. Referring to Fig. 12, it is observed that the greater portion of smaller film

and convergent region of the fluid film helps to spread the hydrodynamic pressure over a larger area along the circumferential direction, with a relatively greater load-carrying capacity than that of a rigid bearing.

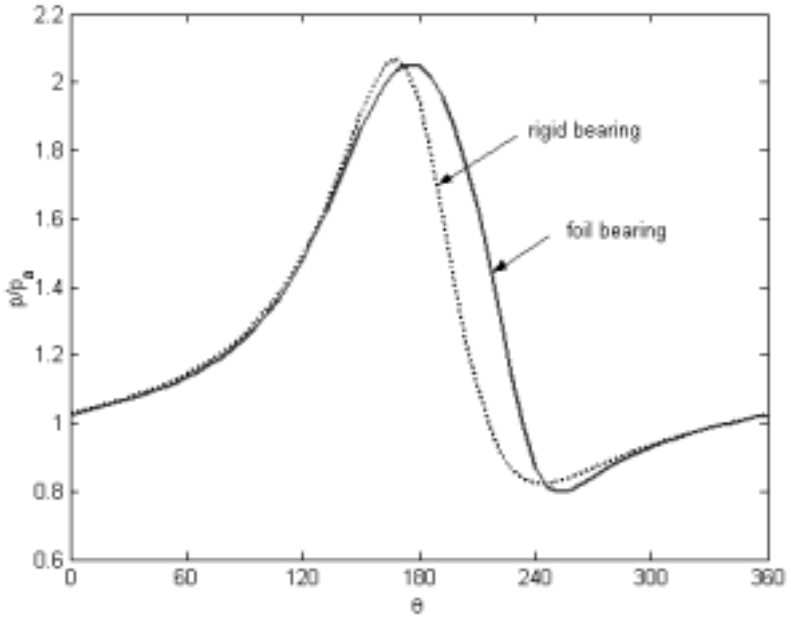

Fig. 13 The mid-plane pressure in a foil bearing compared with that of a rigid bearing

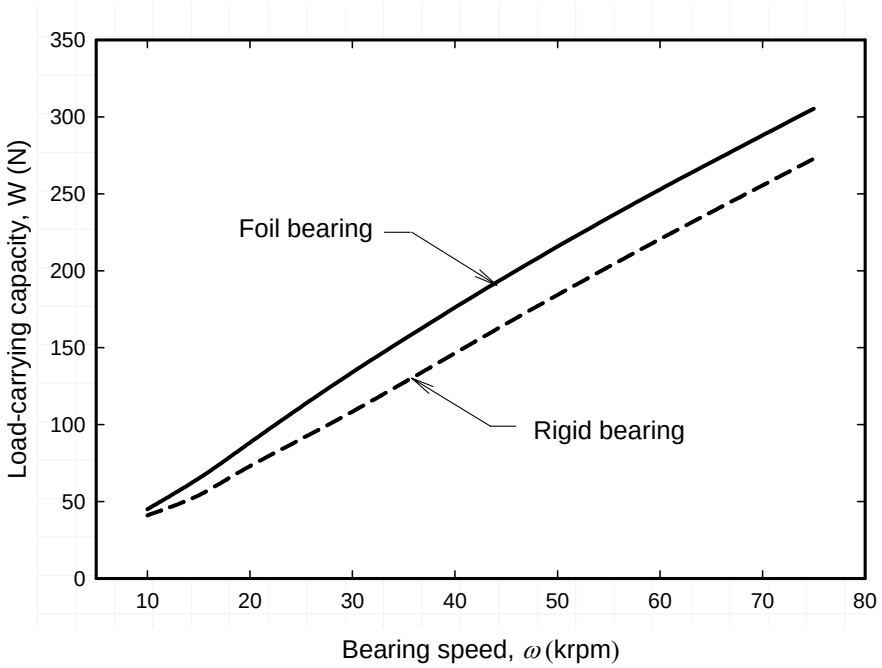

Fig. 14 Load performance of a foil bearing compared with that of a rigid bearing

Fig. 15 shows that in a foil bearing when h_{min} is maintained at a fixed value, the film thickness becomes greater with the increasing speed. Namely, as the speed increases, the film becomes more convergent hence the "lobbing effect" is more pronounced. This is an advantage of a foil bearing over a rigid bearing in terms of bearing stability, because the more pronounced the "lobbing effect," the better is the bearing stability [1]. As we shall explore further, this dynamic film geometry in foil bearings provides just one of many stability advantages of foil bearings over rigid bearings.

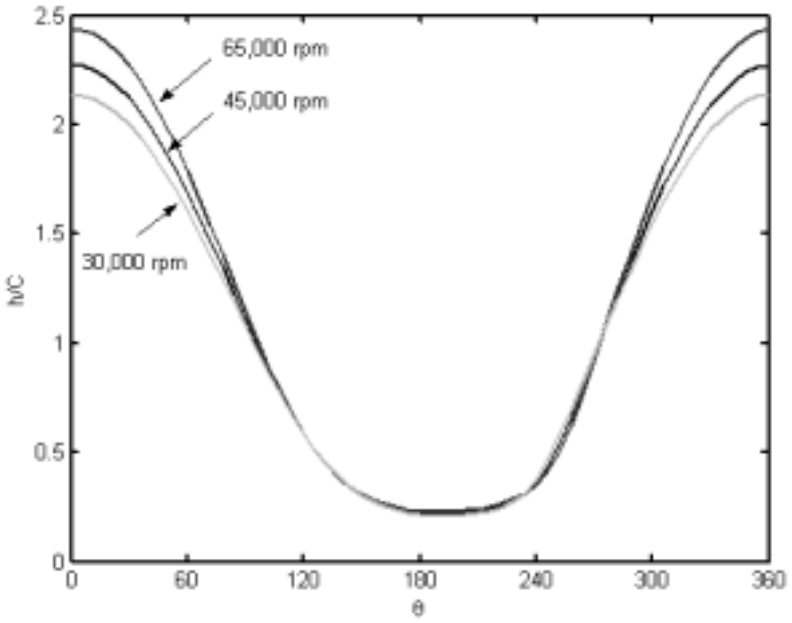

Fig. 15 The increasing film thickness with increasing speeds.

Another important parameter related to the bearing stability is the attitude angle, which is determined by the pressure distribution (see Fig. 5). In general, a smaller attitude angle is considered to result in a better bearing stability. Therefore, it would be interesting to investigate the attitude angle of a foil bearing under various operation conditions. As an example, Fig. 16 is plotted to show the operating attitude angle of a rigid gas bearing and the first generation foil bearing. Both bearings are operating at

60,000 rpm with an assumed h_{min} of 11μm. It is revealed that the attitude angle of the foil bearing is significantly smaller, at about 16°, than that of a rigid bearing, at about 34°.

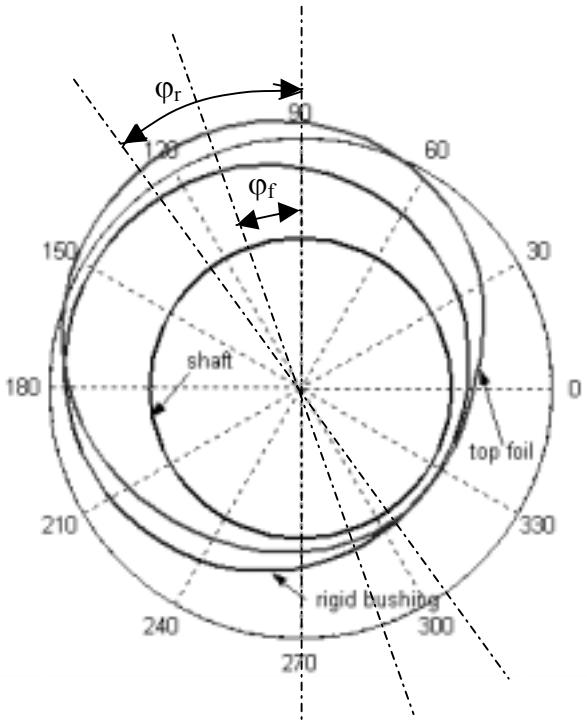

Fig. 16 The comparison of operating attitude angles between rigid bearing and foil bearing

Fig.17 is a comparison of attitude angles between foil bearings and rigid bearings over a large range of speeds. It is shown that the attitude angle of the foil bearing is significantly smaller than that of a rigid bearing throughout the speeds simulated.

In summary, a pronounced convergence of film thickness together with a low attitude angle in a foil bearing at high speeds and high loads tends to improve the dynamic characteristics, particularly from whirl instability viewpoint. This offers a partial explanation for the facts that foil bearings can operate at very high speed without stability problems, whereas the rigid gas bearing of the similar dimension becomes unstable above 14,000 rpm [4].

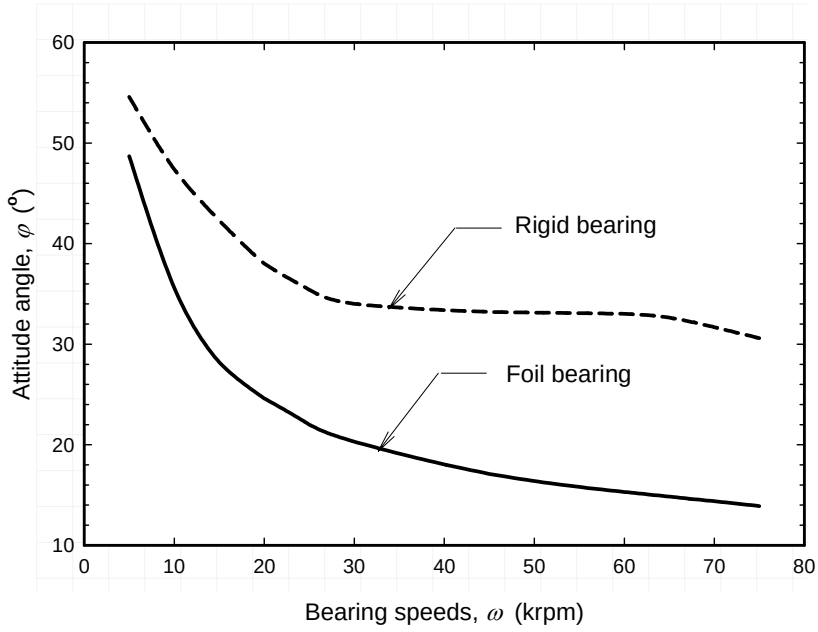

Fig. 17 The attitude angles of a rigid bearing and a foil bearing over a range of speeds

4.3 Characterization of Load Performance at High Speeds

In conventional rigid gas bearing application, numerical simulations show that load-carrying capacity reaches an upper bound as the bearing speed increases [18]. This is suspected to be strongly related to the increasing side leakage with increasing bearing speeds. Bearing surface which determines the fluid film geometry, therefore, is required not only to maximize hydrodynamic pressure but also to minimize leakage. A major difference between conventional rigid gas bearings and foil bearings is that foil bearings have compliant surfaces. During operation the hydrodynamic pressure deforms the foils and that the lubricant film geometry is not fixed. Indeed, it dynamically interacts with fluid film pressure. As bearing speed increases more and more, one expects a larger and larger deviation of foil bearing film geometry from its rigid counterpart. Intuitively, different load performance of foil bearing at high speed is expected.

A series of simulations that cover speed ranges from 50,000 rpm to 1000,000 rpm were carried out and the result is plotted in Fig. 18 to show the different load performance between a rigid bearing and a foil bearing. Both bearings (the same size) are running at a minimum film thickness of h_{min}= 25μm.

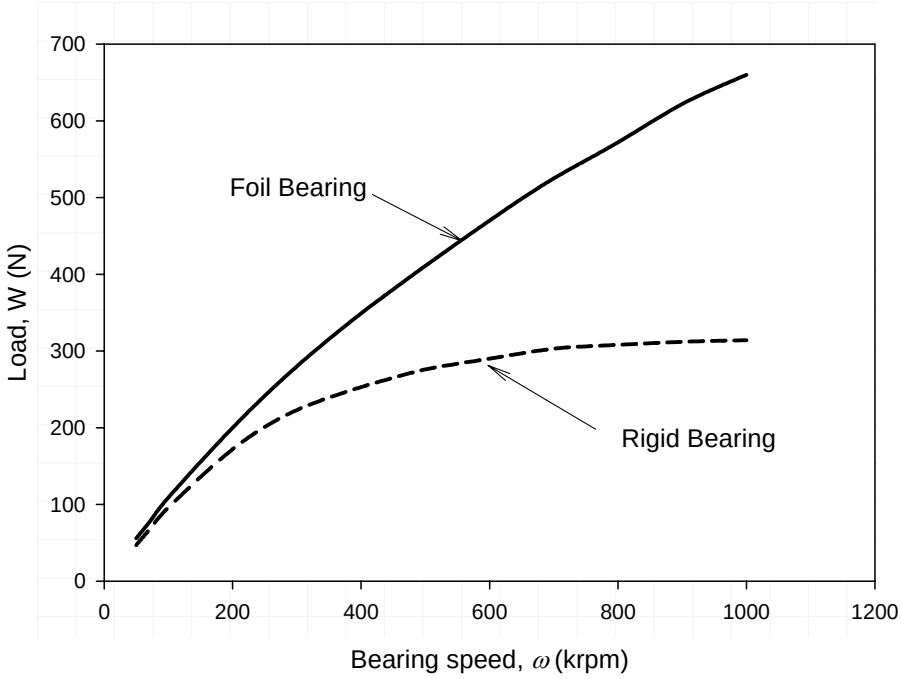

Fig. 18 Comparison of load performance between a foil bearing and a rigid bearing at high speeds

Fig. 18 reveals that while the rigid bearing reaches its upper bound load performance at about 250,000rpm, the foil bearing load capacity keeps increasing within the speed range simulated. This shows another advantage of foil bearing over rigid gas bearing in that substantially high load capacity can be realized by increasing the speed. The numerical results presented in Fig. 18 were verified by the analytical solution derived in section 2.2.

4.4 Conclusions

By numerically solving the compressible Reynolds' equation, predictions on maximum load-carrying capacity are carried out by maintaining reasonable minimum film

thickness. Results were compared with existing experimental data and good agreement has been achieved.

A series of parametric study was carried out for investigating characteristics of foil bearing performance. The simulation systematically predicts the film geometry, pressure distribution, and attitude angle over a large range of operating speed. Foil bearings are predicted to be capable of bearing greater load than their rigid counterparts. In particular, they can achieve substantially higher load-carrying capacity at very high speeds, whereas the rigid bearing reaches upper bound on load capacity after the bearing speed exceeds a certain value.

Foil bearings are also predicted to be able to operate much more stably, because their operating film thicknesses are generally larger and attitude angles are generally smaller than that of rigid bearings. As speed increases the foil bearing film thickness increases. This dynamic feature of fluid film further helps stabilize the bearing performances at high speed. The developed numerical algorithm is shown to be robust in the series parametric study carried out.

CHAPTER5. THERMAL FEATURES AND THE INTERACTION BETWEEN TEMPERATURE AND PRESSURE

5.1 Temperature and Thermal Effect on Pressure

As described in section 2.3, after the pressure field is solved, the pressure work, fluid flow velocities, side flow, and re-circulating flow are calculated and fed into the energy equation, Eq. (3.2.2), to solve for the temperature field. A numerical marching technique with derivative boundary condition for the gas-bushing interface as described in section 3.2 is employed to obtain the temperature field subject to a given inlet temperature and shaft temperature. Since the actual inlet temperature is a mixing temperature between the re-circulating fluid and the fresh fluid that is drawn into the fluid film from the surrounding, and the shaft temperature is the temperature that satisfies the zero net heat flux into the shaft, iteration and bisection search method are used to obtain the final temperature field.

To compare the results of the theoretical analysis against the existing experimental data, two different bearings are considered. Table 3 and Table 4 summarize the appropriate data used for this purposes.

Both bearing 2 and 3 were tested with introduction of cooling air. According to [13], the cooling air was introduced from a feed chamber and flowed through the bearing. Within the bearing, the bulk of the air passed through the bump foil gaps between the top foil and bearing sleeve as well as the operating film thickness. This cooling effect must be incorporated in the analysis by implementing a convective boundary condition with specified heat transfer coefficient, h_{conv}. To estimate h_{conv} using Eq. 2.3.24 and 2.3.25, a simplified model of two parallel plates that represent both the unwrapped operating film

thickness and the unwrapped gap between top foil and bearing sleeve was used to approximate the hydraulic diameter, D_h. The flow of cooling air is assumed laminar.

Table 3 Data of foil bearing 2 (ref. [19])

Shaft radius (R)	50.08×10^{-3} m
Bearing Length (L)	76.2×10^{-3} m
Bump foil stiffness (K_{BS})	6.13×10^{5} N/m
Bump height (H)	0.63×10^{-3} m
Bump foil Yong's Modulus (E)	200×10^{9} N/m^2
Bump foil Poisson's ratio (ν)	0.31
Top foil conductivity (k_T)	60 W/k·m

Table 4 Data of foil bearing 3 (ref. [13])

Shaft radius (R)	36×10^{-3} m
Bearing Length (L)	72×10^{-3} m
Dimensionless foil compliance (α)	1
Bump foil Yong's Modulus (E)	200×10^{9} N/m^2
Bump foil Poisson's ratio (ν)	0.31
Top foil conductivity (k_T)	60 W/k·m

The predictions of the analysis were compared against the experimentally measured data for a series of tests. Table 5 and Table 6 list comparisons of bearing 2 and bearing 3, respectively, between the test results and the predictions. List also in Table 5 and Table 6 are estimated heat transfer coefficients based on assumption. The simulation begins with finding the hydrodynamic pressure and the operating film profile that satisfy

the testing speed and load condition. Accordingly, the flow velocities, side flow, re-circulating flow are calculated. Then all the information obtained is fed into energy equation to solve the temperature distribution and temperature rise. It is revealed by Table 5 and Table 6 that the predicted thermal features of the foil bearing are close to the existing experimental data.

Table 5 Temperature rise in foil bearing 2 (Comparison of experiments with analysis)

Load (N)	Speed (rpm)	Cooling air (m^3/min)	Estimate h_{conv} ($W/m^2 \cdot K$)	ΔT_{exp} (C)	$\Delta T_{analysis}$ (C)
396	2500	0.85	60	32.2	30.0
760	2000	1.13	80	35	36.2
1005	3000	1.33	100	44.4	50.7

Table 6 Temperature rise in foil bearing 3 (Comparison of experiments with analysis)

Load (N)	Speed (rpm)	Cooling air (m^3/min)	Estimate h_{conv} ($W/m^2 \cdot K$)	ΔT_{exp} (C)	$\Delta T_{analysis}$ (C)
356	1500	0.85	60	32	27.5
934	2000	0.8	60	81	84.2
1334	3000	1.36	160	57	49.0

As an example, the predicted temperature distribution of the fluid film when bearing 2 runs at the speed of 20,000 rpm with 760N load is plotted in Fig. 19. The inlet temperature converges to about 26°C and shaft temperature converges to about 58°C. Note that in this case the temperature profile ends at about $\theta = 246°$, where the pressure becomes "negative". This is the predicted point where the fresh cold air starts to enter the bearing and mixes with the re-circulating hot air.

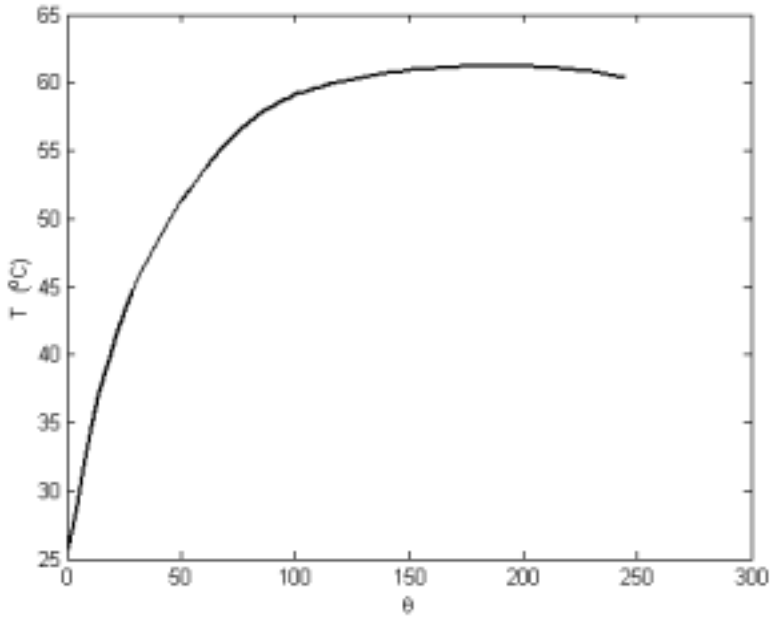

Fig. 19 Temperature rise of bearing 2 running at 20,000rpm

As an example of the prediction on the temperature distribution of bearing 3, shown in Fig. 20 is the analysis on bearing 3 at 20,000 rpm. The tested bearing was operating under 934N load and the analysis predicts an operational eccentricity ratio to be greater than unit. With a dramatically deformed top foil and that very small minimum film thickness h_{min}, the analysis predicts an inlet temperature of about 67°C and a shaft temperature of about 100°C.

A series of simulation results on the temperature rise of bearing 1 at speeds from 15,000 rpm to 65,000 rpm are plotted in Fig. 21. Due to the lack of cooling air during the test on bearing 1 for load performance, an arbitrary value for heat transfer coefficient h_{conv} = 45 was used in the simulations. The detailed information of two operating conditions of bearing 1 is listed in Table 7 and 8 to show the comparison among isothermal theory, THD theory, and experimental data.

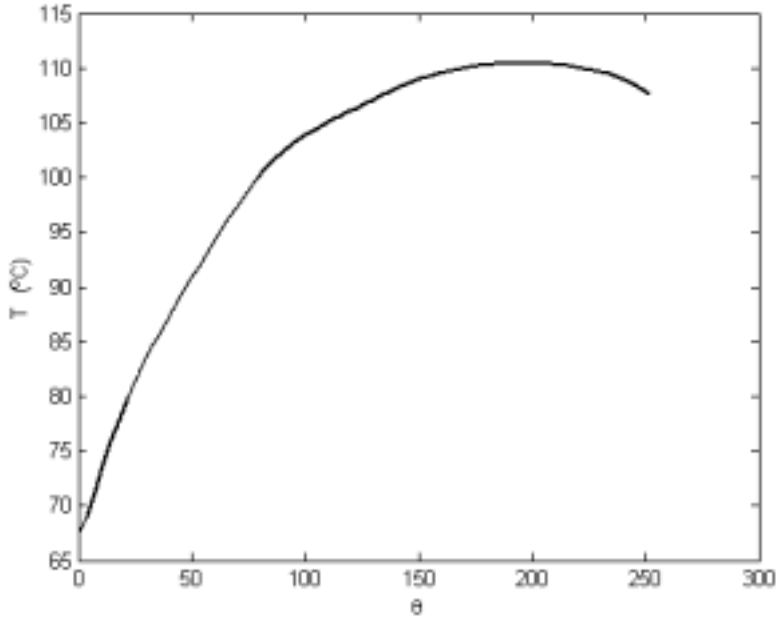

Fig. 20 Temperature rise of bearing 3 running at 20,000rpm

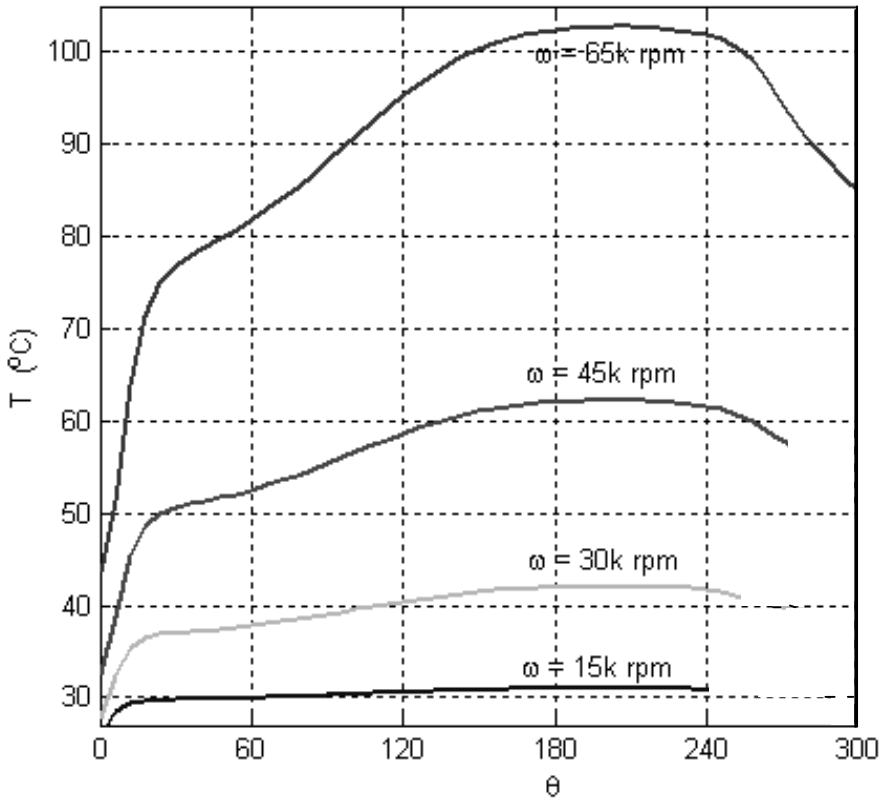

Fig. 21 Temperature rise of bearing 1 at different speeds.

Table 7 Performance of foil bearing 1 at 30,000 rpm

Performance	Experiment	Isothermal Theory	THD Theory
Eccentricity ratio		1.12	1.15
Load (N)	130	137.2	140.5
P_{max}/P_a		2.03	2.10
Attitude angle (°)		22.3	19.8
Q_{leak} (m^2/sec)		1.95×10^{-4}	2.07×10^{-4}
T_{shaft} (°C)			36.5
T_{max} (°C)			38.4

Table 8 Performance of foil bearing 1 at 45,000 rpm

Performance	Experiment	Isothermal Theory	THD Theory
Eccentricity ratio		1.26	1.28
Load (N)	210	216.2	227.2
P_{max}/P_a		2.45	2.53
Attitude angle (°)		18.5	17.6
Q_{leak} (m^2/sec)		3.76×10^{-4}	4.38×10^{-4}
T_{shaft} (°C)			51.9
T_{max} (°C)			62.3

As revealed in Fig. 21, when the bearing operates at 65,000 rpm the gas temperature is predicted to reach about 100°C and that thermal effect shall play significant role on hydrodynamic pressure. Shown in Fig. 22 is a comparison of 3-D pressure between isothermal analysis and THD analysis when bearing 1 whose data is

tabulated in Table 1 runs at 65,000 rpm. Fig. 22 reveals that hydrodynamic pressure of gas film increases with increasing gas temperature.

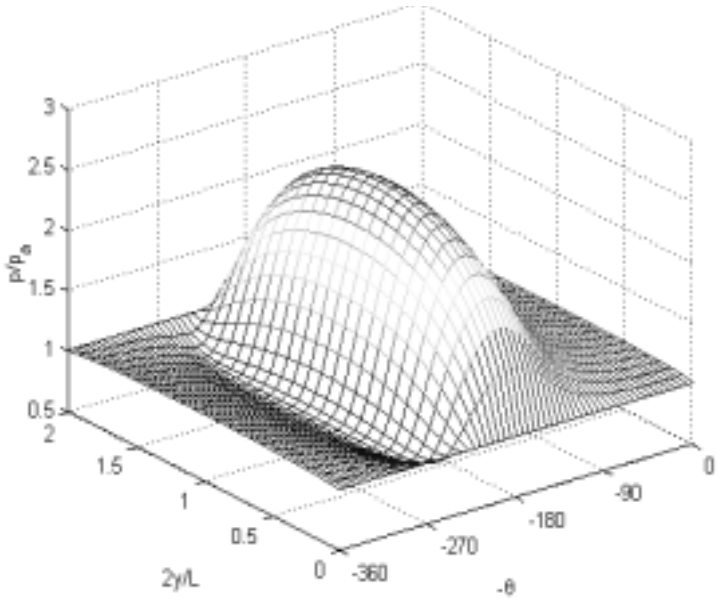

Fig. 22a. Pressure profile of bearing 1 at 65,000 rpm using isothermal theory

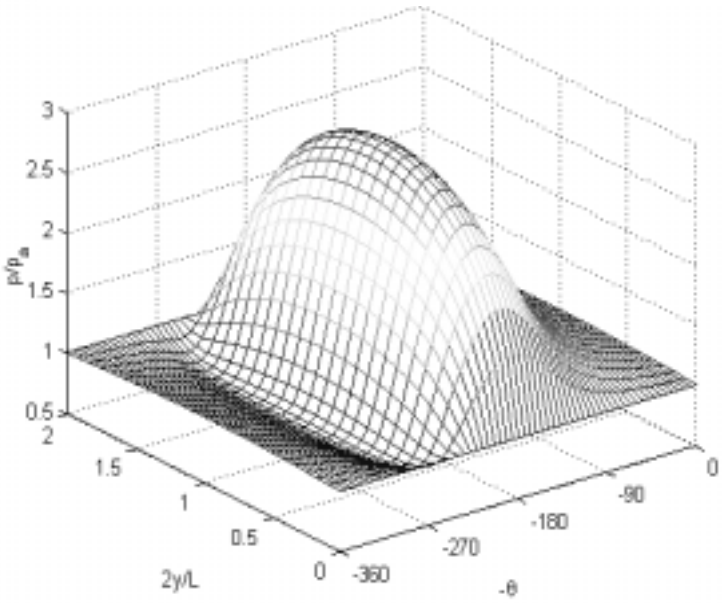

Fig. 22b . Pressure profile of bearing 1 at 65,000 rpm using THD theory

5.2 The Effect of Pressure Work on Temperature Rise and Distribution

In section 5.1, we showed the thermal effect has a major influence on the hydrodynamic pressure. In this section, we explore the effect of pressure work on the temperature field. The major difference in energy equation for compressible fluid and incompressible fluid is the pressure work term. For an incompressible fluid lubricated bearing, the pressure work is negligible. In contrast, the pressure work in a compressible fluid lubricated bearing is important. This is particularly interesting for a journal type bearing, because the compressible gas experiences compression and expansion cycles as the shaft runs on top of it. When the gas is compressed in the convergent region of the film, it does positive work and releases heat; while in the divergent region, the gas expands and absorbs heat. For the parametric study purpose, we compare the temperature resulting from considering the pressure work term in the energy equation and setting the pressure work term to zero. Fig. 23 shows an example of this analysis for bearing 3.

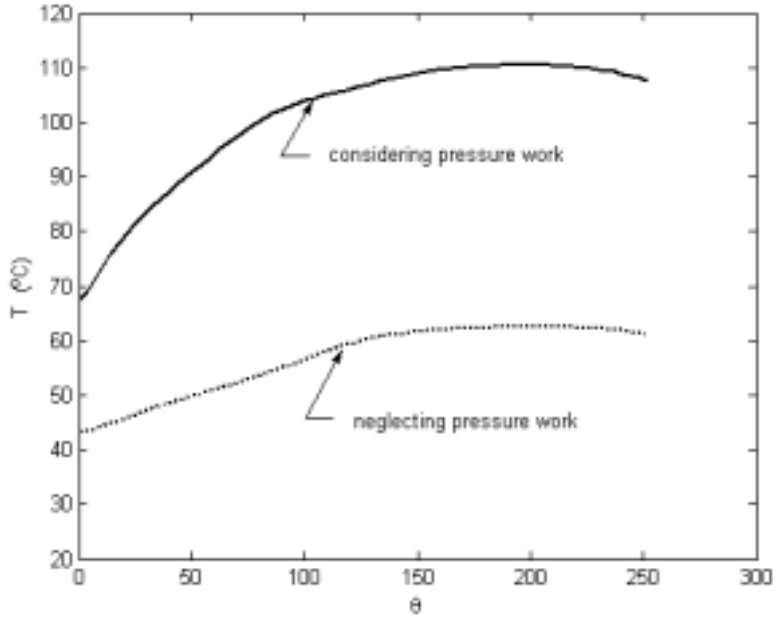

Fig. 23 The effect of pressure work on temperature rise and distribution

The bearing runs at 20,000 rpm with load of 934 N and a heat transfer coefficient of 60 $W/m^2 \cdot K$ is assumed. It is revealed that the pressure work contributes significantly to the temperature rise: the overall temperature rise is about 85°C, while the pressure work contributes 48°C.

5.3 Conclusions

A thermo-hydrodynamic (THD) analysis of foil bearing with considering the effect of bearing compliance and the compressibility of the lubricant is presented. The compressible Reynolds' equation and the Energy equation were solved simultaneously in an iterative scheme by multiple couplings among the system of equations through the density and viscosity of the lubricant, pressure work, and the fluid film geometry. The predicted temperature rise of several foil bearings within a large range of speeds matches the existing experimental data. The model predicts that increasing temperature increases the hydrodynamic pressure of the gas film in foil bearings. The investigation on the role of the fluid pressure work in foil bearings reveals that it plays significant role on temperature rise and temperature distribution of the fluid film.

BIBLIOGRAPHY

1 Heshmat, H., 1994, "Advancements in the Performance of Aerodynamic Foil Journal Bearings: High Speed and Load Capacity", Journal of Tribology, Vol. 116, pp287-295.

2 Dellacorte, C. 1997, "A new Foil Air Bearing Test Rig for Use to 700 C and 70,000 rpm", NASA Technical Memorandum 107405.

3 DellaCorte, C., Lukaszewicz, V., Valco, M. J., Radil, K. C., and Heshmat, H., 2000, "Performance and Durability of High Temperature Foil Air Bearings for Oil-Frell Turbomachinery", NASA/TM-2000-209187/Rev1, ARL-TR-2202.

4 DellaCorte, C. and Valco, M. J., 2000, "Load Capacity Estimation of Foil Air Journal Bearings for Oil-Free Turbo-machinery Applications", NASA/TM-200-209782, ARL-TR-2334.

5 Heshmat, H., 1991, "Analysis of Compliant Foil Bearing With Spatially Variable Stiffness", AIAA-91-2102-CP.

6 DellaCorte, C., 2000, "The Evaluation of a Modified Chrome Oxide Based High Temperature Solid Lubricant Coating for Foil Gas Bearing", Tribology Transactions, V. 43, 2, pp257-262.

7 Heshmat H., Walowit J. A., and Pinkus O., 1983, "Analysis of Gas-Lubricated Foil Journal Bearings", Journal of Lubrication Technology, Vol. 105, pp. 647-655.

8 Khonsari M., and Booser E., 2001, Applied Tribology, John Wiley & Sons. Inc.

9 Harmrock, B. J., 1994, Fundamentals of Fluid Film Lubrication, McGraw-Hill Inc.

10 Dowson, D., Hudson, J. D., Hunter, B. and March, C. N., 1966 "An Experimental Investigation of the Thermal Equilibrium of Steadily Loaded Journal Bearings," Proceedings Institutions of Mechanical Engineers (London), V. 181, pt. 3B, pp. 70-80.

11 Khonsari, M. M., Jang J. Y., and Fillon. M., 1996, "On the Generalization of Thermohydrodynamic Analyses for Journal Bearings", Journal of Tribology, V 118, pp571-579;

12 Dowson, D., 1962, "A Generalized Reynolds Equation for Fluid-Film Lubrication", International Journal of Mechanical Engineering Sciences, V. 4, pp. 159-170;

13 Salehi M., Swanson E., and Heshmat H., 2001, "Thermal Features of Compliant Foil Bearings — Theory and Experiments", Journal of Tribology, Vol. 123, pp566-571.

14 Khonsari, M. M. and Beaman, J. J., 1986, "Thermohydrodynamic Analysis of Laminar Incompressible Journal Bearings", ASLE Transactions, V. 29, pp141-150.

15 Ezzat, H. A., and Rhode, S. M., 1973, "A Study of the Thermohydrodynamic Performance of Finite Slide Bearing," ASME Journal of Lubrication Technology, pp298-307;

16 Gerald C. F. and Wheatley P. O., 1989, Applied Numerical Anlysis (4^{th} Edition), Addison-Wesley.

17 Advanced Gas Turbine (AGT) Technology Development Project-Final Report, NASA CR-180891, December 1987. T. Strom Program Manager.

18 Faria, M. T. and San Andres, L., 2000, "On the Numerical Modeling of High-speed Hydrodynamic Gas Bearing", Transactions of the ASME, V. 122, pp124-130.

19 Salehi M. and Heshmat H., 2000, "On the Fluid Flow and Thermal Analysis of a Compliant Surface Foil Bearing and Seal", Tribology Tansactions, Vol. 43, pp318-324.

APPENDEX A ON THE BOUNDARY CONDITIONS OF FOIL JOURNAL BEARINGS

The energy equation, Eq.(2.3.11) in section 2.3, is repeated below for convenience:

$$\bar{\rho}\left(\bar{u}\frac{\partial \bar{T}}{\partial \theta}+\frac{1}{\bar{h}}\bar{w}\frac{\partial \bar{T}}{\partial \bar{z}}\right)=\frac{\kappa_1}{\kappa_2^2}\frac{1}{\bar{h}^2}\frac{\partial^2 \bar{T}}{\partial \bar{z}^2}+\bar{u}\kappa_3\frac{d\bar{p}_\theta}{d\theta} + \kappa_1\frac{\bar{T}}{\bar{h}^2}\left(\frac{\partial \bar{u}}{\partial \bar{z}}\right)^2+\kappa_1\frac{1}{\bar{h}^2}\left(\frac{\partial \bar{u}}{\partial \bar{z}}\right)^2 \tag{A.1}$$

The appropriate boundary conditions to Eq. (A.1) are:

$$\begin{aligned}
&\bar{T}(0,\bar{z})=\bar{T}_i(\bar{z})\\
&\bar{T}(\bar{x},1)=\bar{T}_s\\
&\bar{T}(\bar{x},0)=\bar{T}_B(\bar{x},R+h)\\
&-k\frac{1}{h}\frac{\partial \bar{T}}{\partial \bar{z}}\bigg|_{\bar{z}=0}=k_B\frac{\partial \bar{T}_B}{\partial r}\bigg|_{r=R+h}
\end{aligned} \tag{A.2}$$

In order to match the temperature of the lubricant to the temperature of the bearing, one must find the bearing temperature that satisfies the system.

$$\frac{1}{r}\frac{\partial}{\partial r}\left(r\frac{\partial \bar{T}_B}{\partial r}\right)+\frac{1}{r^2}\frac{\partial^2 \bar{T}_B}{\partial \theta^2}=0 \tag{A.3}$$

In the foil bearing application, the top foil is very thin and that the heat conduction in circumferential direction would be small compared with radial heat conduction. Neglecting circumferential heat flow in the bearing will lead to significant simplification in the computational scheme, for in this case Eq. (A.3) becomes:

$$\frac{1}{r}\frac{\partial}{\partial r}\left(r\frac{\partial \bar{T}_B}{\partial r}\right)=0\,, \tag{A.4}$$

which can be integrated directly.

The boundary conditions appropriate to Eq. (A.4) are:

$$k_B \left.\frac{\partial \overline{T}_B}{\partial r}\right|_{r=R+h} = -k \frac{1}{h} \left.\frac{\partial \overline{T}}{\partial \overline{z}}\right|_{\overline{z}=0}$$

$$-k_B \left.\frac{\partial \overline{T}_B}{\partial r}\right|_{r=R+h+t_B} = \mathrm{h}_{\mathrm{conv}} \overline{T}_B(\theta, R+h+t_B) \tag{A.5}$$

$$\overline{T}_B(\overline{x}, R+h) = \overline{T}(\overline{x}, 0)$$

The first and the third of Eq. (A.5) are the matching conditions already quoted in Eq. (A.2).

Now with Eq. (A.1), (A.2), (A.4), and (A.5), one can use iteration scheme to solve two temperature fields in two-dimensional film region and across the top foil.

Nevertheless, since our most interest of temperature is the film/top-foil interface, which can be obtained from any one of the energy equations, a simpler way to reach this objective is derived in the following way.

Integrating Eq. (A.4), we have

$$\overline{T}_B = C_1 \ln r + C_2 \tag{A.6}$$

where C_1 and C_2 are constants.

therefore,

$$\overline{T}_B(\overline{x}, R+h) = C_1 \ln(R+h) + C_2,$$

$$\overline{T}_B(\overline{x}, R+h+t_B) = C_1 \ln(R+h+t_B) + C_2$$

$$\left.\frac{\partial \overline{T}_B}{\partial r}\right|_{r=R+h} = \frac{C_1}{R+h}, \tag{A.7}$$

$$\left.\frac{\partial \overline{T}_B}{\partial r}\right|_{r=R+h+t_B} = \frac{C_1}{R+h+t_B}$$

Substitute Eq. (A.7) into Eq. (A.5) yields

$$k_B \frac{C_1}{R+h} = -k \frac{1}{h} \frac{\partial \overline{T}}{\partial \overline{z}}\bigg|_{\overline{z}=0}$$

$$-k_B \frac{C_1}{R+h+t_B} = \mathrm{h}_{\mathrm{conv}}\left[C_1 \ln(R+h+t_B) + C_2\right] \tag{A.8}$$

$$C_1 \ln R + C_2 = \overline{T}(\overline{x},0)$$

Solving for C_1 and C_2 from the first two of Eq. (A.8), we have:

$$\begin{aligned} C_1 &= -(R+h)\frac{k}{k_B}\frac{1}{h}\frac{\partial \overline{T}}{\partial \overline{z}}\bigg|_{\overline{z}=0} \\ C_2 &= (R+h)\frac{1}{h}\frac{\partial \overline{T}}{\partial \overline{z}}\bigg|_{\overline{z}=0}\left[\frac{k}{\mathrm{h}_{\mathrm{conv}}(R+h+t_B)} + \frac{k}{k_B}\ln(R+h+t_B)\right] \end{aligned} \tag{A.9}$$

Substitution of Eq. (A.9) into the third condition of Eq. (A.8) yields the relationship:

$$\left(\overline{T} + \gamma \frac{\partial \overline{T}}{\partial \overline{z}}\right)_{\overline{z}=0} = 0 \tag{A.10}$$

where

$$\gamma(\theta) = -\left[1 + \frac{1}{\overline{h}(\theta)}\left(\frac{R}{C}\right)\right]\left[\frac{1}{\aleph(\theta)} + \frac{k}{k_B}\ln\left(1 + \frac{t_B}{R + C\overline{h}(\theta)}\right)\right] \tag{A.11}$$

here the Nusselt is defined as

$$\aleph(\theta) = \frac{\mathrm{h}_{\mathrm{conv}}\left(R + C\overline{h}(\theta) + t_B\right)}{k} \tag{A.12}$$

where *k* is the conductivity of the lubricant media, not as in the most common definition of Nusselt number where *k* is the conductivity of the convective fluid around the bushing. Eq. (A.11) now replaces the matching conditions and it is no longer necessary to find solution of Eq. (A.4) and subjecting it to Eq. (A.5); instead it will suffice to solve only Eq. (A.1) with the following initial and homogeneous boundary conditions:

$$\overline{T}(0,\bar{z}) = \overline{T}_i(\bar{z})$$
$$\overline{T}(\bar{x},1) = \overline{T}_s \qquad \text{(A.13)}$$
$$\left(\overline{T} + \gamma \frac{\partial \overline{T}}{\partial \bar{z}}\right)_{\bar{z}=0} = 0$$

APPENDEX B DOCUMENTATION ON MATLAB PROGRAMS

Main Program:

```
load inputdata.txt;
omega=30000*2*pi/60;
epsilon=.775;
h=1+epsilon*cos(theta);
m=20;
n=100;
mn=20;
dy=1/m;
y=[0:dy:1];
dtheta=2*pi/n;
theta=[0:dtheta:n*dtheta];
dz=1/mn;
z=[0:dz:1];
Lambda=6*mu0*omega/p0*(R/C)^2;
lambda1=rho0*cp*R^2*omega/k;
lambda2=(R/C)^2;
lambda3=p0*R^2*omega/(k*tao0);
lambda4=(R/C)^2*a*(R*omega)^2/k;
kapa1=lambda4/lambda1;
kapa2=sqrt(lambda4/lambda2);
kapa3=lambda3/lambda1;
```

```
for i=1:m+1,
   hh(i,:)=h;
end;
mubar=1.*ones(1,n+1);
p1 = incompres(Lambda, epsilon, mubar, h, n, dtheta);
pmax=max(p1);
for i=1:n/2+1,
   p(i)=-(pmax-1)/(n/2)^2*(i-1)^2+2*(pmax-1)/(n/2)*(i-1)+1;
end;
for i=n/2+2:n+1,
   p(i)=p(n+2-i);
end;
for i=1:m+1,
   pp_guess(i,:)=-(p-1)/(m)^2*(i-1)^2+2*(p-1)/(m)*(i-1)+1;
end;
[pp, dpx, dpy] = compres(D, L, Lambda, mubar, hh, pp_guess, m, n, dy, dtheta);
ppL=pp;
for i=m+2:2*m+1
   ppL(i,:)=ppL(2*m+2-i,:);
end;
[W, phi] = load(ppL,theta,dtheta,dy,p0,R,L,m,n);
```

```
[pp1, hh1, dpx1, dpy1] = compliant(D, L, alpha, Lambda, epsilon, mubar, h, hh, pp, m, n,
dy, dtheta, theta);
[pp2, hh2, dpx2, dpy2, epsilon1] = Eccentric(D, L, alpha, Lambda, epsilon, mubar, h, hh,
hh1, pp, pp1, m, n, dy, dtheta, theta);
ppL2=pp2;
for i=m+2:2*m+1
  ppL2(i,:)=ppL2(2*m+2-i,:);
end;
[W2, phi_2] = load(ppL2,theta,dtheta,dy,p0,R,L,m,n);
[Qleak, Qsuck, Qrec, P_mid, cav] = FlowRate(omega, R, D, L, C, p0, mu0, mubar, pp,
hh, dpx, dpy, m, n, dy, dtheta);
[Ts,Ti,T,rho1] = energy(KK, T0, H, tb, k, kb, omega, epsilon, R, C, p0, mu0, mubar, h2,
pp2, P_mid, cav, Qleak, Qsuck, Qrec,kapa1,kapa2,kapa3, n, mn, dy, dtheta, dz,z);
for j=1:n+1,
  mubar1(j)=a*tao0*(1+mean((T(:,j))))/mu0;
end;
while abs(norm(mubar1)-norm(mubar))/norm(mubar1)>1e-3;
  mubar=mubar1;
  for j=1:n+1
     T(j)=1+tao0/T0*mean(T(:,j));
  end;
  [pp_THD, dpx, dpy] = compres2(T, D, L, Lambda, mubar, hh, pp, m, n, dy, dtheta);
```

```
  [pp1_THD, hh1_THD, dpx1, dpy1] = compliant2(T, D, L, alpha, Lambda, epsilon, mubar1, hh, pp_THD, m, n, dy, dtheta, theta);
  [pp2_THD, hh2_THD, dpx2, dpy2, epsilon1_THD] = Eccentric2(T, D, L, alpha, Lambda, epsilon, mubar1, hh, pp_THD, pp1_THD, m, n, dy, dtheta, theta);
  [Qleak_THD, Qsuck_THD, Qrec_THD, P_mid_THD, cav_THD] = FlowRate(omega, R, D, L, C, p0, mu0, mubar1, pp2_THD, hh2_THD, dpx2, dpy2, m, n, dy, dtheta);
  [Ts,Ti,T,rho2] = energy(KK, T0, H, tb, k, kb, omega, epsilon, R, C, p0, mu0, mubar1, h2_THD, pp2_THD, P_mid_THD, cav_THD, Qleak_THD, Qsuck_THD, Qrec_THD, kapa1, kapa2, kapa3, n, mn, dy, dtheta, dz, z);
  for j=1:n+1,
     mubar1(j)=a*tao0*(1+mean((T(:,j))))/mu0;
  end;
end;
ppL2_THD=pp2_THD;
for i=m+2:2*m+1
   ppL2_THD(i,:)=ppL2_THD(2*m+2-i,:);
end;
[W2_THD, phi_2_THD]=load(ppL2_THD,theta,dtheta,dy,p0,R,L,m,n);
figure(1);plot(theta*180/pi,pp(m+1,:),'b');hold on;
figure(1);plot(theta*180/pi,pp2(m+1,:),'b');hold on;
figure(1);plot(theta*180/pi,pp2_THD(m+1,:),'r:');
figure(2);plot(theta*180/pi,hh(m+1,:),'b');hold on;
figure(2);plot(theta*180/pi,hh2(m+1,:),'r');hold on;
```

```
figure(2);plot(theta*180/pi,hh2_THD(m+1,:),'r');
for i=1:2*m+1,
   for j=1:n+1,
      ppL_rev(i,j)=ppL(2*m+2-i,n+2-j);
      ppL2_rev(i,j)=ppL2(2*m+2-i,n+2-j);
      ppL2_THD_rev(i,j)=ppL2_THD(2*m+2-i,n+2-j);
   end;
end;
yy=[0:dy:2];
figure(3);mesh(theta*180/pi,yy,ppL_rev);
figure(4);mesh(theta*180/pi,yy,ppL2_rev);
figure(5);mesh(theta*180/pi,yy,ppL2_THD_rev);
figure(6),plot(theta*180/pi,T2(mn/2,:)*tao0+T0,'r')
return;
```

Subroutines:

(1) Input data

```
R=19.05e-3;
D=2*R;
C=50e-6;
L=38.1e-3;
rho0=1.1614;
cp=1007;
k=26.3e-3;
```

```
mu0=184.6e-7;

p0=101000;

t=0.1016e-3;

s=4.572e-3;

l=1.778e-3;

E=200e9;

v=0.31;

alpha=2*p0*s/(C*E)*(l/t)^3*(1-v^2);

a=4e-8;

KK=-458.75;

T0=25;

tao0=T0-KK;

H=120;

kb=60;

tb=2*t;
```

(2) Incompressible Reynolds equation

```
function pbar1 = incompres(Lambda, epsilon, mubar, h, n, dtheta);

hbar1=h;

for j=1:2

  xl(j)=(j-1)*pi;

  xr(j)=j*pi;

  step(j)=0;

  while abs(xr(j)-xl(j))>10^(-12)
```

```
x(j)=1/2*(xl(j)+xr(j));
int2xr=0;
      for i=1:floor(n*xr(j)/(2*pi))
            int2xr=int2xr+1/hbar1(i)^2*dtheta;
      end;
      int3xr=0;
      for i=1:floor(n*xr(j)/(2*pi))
            int3xr=int3xr+1/hbar1(i)^3*dtheta;
end;
int2x=0;
      for i=1:floor(n*x(j)/(2*pi))
            int2x=int2x+1/hbar1(i)^2*dtheta;
end;
      int3x=0;
      for i=1:floor(n*x(j)/(2*pi))
            int3x=int3x+1/hbar1(i)^3*dtheta;
      end;
if (int2xr-(1+epsilon*cos(xr(j)))*int3xr)*...
            (int2x-(1+epsilon*cos(x(j)))*int3x)>0
   xr(j)=x(j);
else
   xl(j)=x(j);
end;
```

```
      step(j)=step(j)+1;
   end;
end;
x1=x(1,2);
thetacav1=x1;
int2=0;
int21(1,1)=0;
for i=1:floor(n*thetacav1/(2*pi))
   int2=int2+1/hbar1(i)^2*dtheta;
   int21(1,i+1)=int2;
end;
int3=0;
int31(1,1)=0;
for i=1:floor(n*thetacav1/(2*pi))
   int3=int3+1/hbar1(i)^3*dtheta;
   int31(1,i+1)=int3;
end;
for i=1:floor(n*thetacav1/(2*pi))
    pbar1(i)=mubar(i)*Lambda*int21(i)-
mubar(i)*Lambda*(1+epsilon*cos(thetacav1))*int31(i)+1;
end;
m=size(pbar1);
pbar1=[pbar1 ones(1,n+1-m(1,2))];
```

(3) Compressible Reynolds' equation

```
function [ppn, dpx, dpy] = compres(D, L, Lambda, mubar, hh, pp, m, n, dy, dtheta);
for i=1:m+1,
   dpx(i,1)=-(3*pp(i,1)-4*pp(i,2)+pp(i,3))/2/dtheta;
   for j=2:n
      dpx(i,j)=(pp(i,j+1)-pp(i,j-1))/2/dtheta;
   end;
   dpx(i,n+1)=dpx(i,1);
end;
for j=1:n+1,
   dpy(1,j)=-(3*pp(1,j)-4*pp(2,j)+pp(3,j))/2/dy;
   for i=2:m
      dpy(i,j)=(pp(i+1,j)-pp(i-1,j))/2/dy;
   end;
   dpy(m+1,j)=0;
end;
for i=1:m+1,
   dhx(i,1)=-(3*hh(i,1)-4*hh(i,2)+hh(i,3))/2/dtheta;
   for j=2:n
      dhx(i,j)=(hh(i,j+1)-hh(i,j-1))/2/dtheta;
   end;
   dhx(i,n+1)=-dhx(i,1);
end;
```

```
for j=1:n+1,
   dhy(1,j)=-(3*hh(1,j)-4*hh(2,j)+hh(3,j))/2/dy;
   for i=2:m
      dhy(i,j)=(hh(i+1,j)-hh(i-1,j))/2/dy;
   end;
   dhy(m+1,j)=0;
end;
for i=1:m+1,
   for j=1:n+1,
      f(i,j)=-1/pp(i,j)*(dpx(i,j)^2+(D/L)^2*dpy(i,j)^2)-
3/hh(i,j)*(dhx(i,j)*dpx(i,j)+dhy(i,j)*dpy(i,j))+mubar(j)*Lambda/hh(i,j)^2/pp(i,j)*dpx(i,j)
         +mubar(j)*Lambda/hh(i,j)^3*dhx(i,j);
      %f(i,j)=-1/pp(i,j)*(dpx(i,j)^2+(D/L)^2*dpy(i,j)^2)-(3/hh(i,j)*dhx(i,j)-
mubar(j)*Lambda/hh(i,j)^2/pp(i,j))*dpx(i,j)...
         %+mubar(j)*Lambda/hh(i,j)^3*dhx(i,j);
      %f(i,j)=mubar(j)*Lambda/hh(i,j)^3*dhx(i,j);
   end;
end;
omega=1.;
ppn(1,:)=ones(1,n+1);
for i=2:m+1,
   for j=1:n+1
      if j==1
```

```
        if i==m+1
            ppn(i,j)=pp(i,j)+omega*((L/D)^2*dy^2*(pp(i-1,j)+pp(i-
1,j))+dtheta^2*(pp(i,j+1)+pp(i,n))...
                -2*(dtheta^2+(L/D)^2*dy^2)*pp(i,j)-
dtheta^2*(L/D)^2*dy^2*f(i,j))/(2*(dtheta^2+(L/D)^2*dy^2));
        else
            ppn(i,j)=pp(i,j)+omega*((L/D)^2*dy^2*(pp(i+1,j)+pp(i-
1,j))+dtheta^2*(pp(i,j+1)+pp(i,n))...
                -2*(dtheta^2+(L/D)^2*dy^2)*pp(i,j)-
dtheta^2*(L/D)^2*dy^2*f(i,j))/(2*(dtheta^2+(L/D)^2*dy^2));
        end;
        elseif j==n+1
        if i==m+1
            ppn(i,j)=pp(i,j)+omega*((L/D)^2*dy^2*(pp(i-1,j)+pp(i-
1,j))+dtheta^2*(pp(i,2)+pp(i,j-1))...
                -2*(dtheta^2+(L/D)^2*dy^2)*pp(i,j)-
dtheta^2*(L/D)^2*dy^2*f(i,j))/(2*(dtheta^2+(L/D)^2*dy^2));
        else
            ppn(i,j)=pp(i,j)+omega*((L/D)^2*dy^2*(pp(i+1,j)+pp(i-
1,j))+dtheta^2*(pp(i,2)+pp(i,j-1))...
                -2*(dtheta^2+(L/D)^2*dy^2)*pp(i,j)-
dtheta^2*(L/D)^2*dy^2*f(i,j))/(2*(dtheta^2+(L/D)^2*dy^2));
        end;
```

```
        else
            if i==m+1
                ppn(i,j)=pp(i,j)+omega*((L/D)^2*dy^2*(pp(i-1,j)+pp(i-
1,j))+dtheta^2*(pp(i,j+1)+pp(i,j-1))...
                    -2*(dtheta^2+(L/D)^2*dy^2)*pp(i,j)-
dtheta^2*(L/D)^2*dy^2*f(i,j))/(2*(dtheta^2+(L/D)^2*dy^2));
            else
                ppn(i,j)=pp(i,j)+omega*((L/D)^2*dy^2*(pp(i+1,j)+pp(i-
1,j))+dtheta^2*(pp(i,j+1)+pp(i,j-1))...
                    -2*(dtheta^2+(L/D)^2*dy^2)*pp(i,j)-
dtheta^2*(L/D)^2*dy^2*f(i,j))/(2*(dtheta^2+(L/D)^2*dy^2));
            end
        end;
    end;
end;
while abs(norm(ppn)-norm(pp))/abs(norm(ppn))>1e-4,
pp=ppn;
for i=1:m+1,
    dpx(i,1)=-(3*pp(i,1)-4*pp(i,2)+pp(i,3))/2/dtheta;
    for j=2:n
        dpx(i,j)=(pp(i,j+1)-pp(i,j-1))/2/dtheta;
    end;
    dpx(i,n+1)=dpx(i,1);
```

```
end;
for j=1:n+1,
   dpy(1,j)=-(3*pp(1,j)-4*pp(2,j)+pp(3,j))/2/dy;
   for i=2:m
      dpy(i,j)=(pp(i+1,j)-pp(i-1,j))/2/dy;
   end;
   dpy(m+1,j)=0;
end;
for i=1:m+1,
   dhx(i,1)=-(3*hh(i,1)-4*hh(i,2)+hh(i,3))/2/dtheta;
   for j=2:n
      dhx(i,j)=(hh(i,j+1)-hh(i,j-1))/2/dtheta;
   end;
   dhx(i,n+1)=-dhx(i,1);
end;
for j=1:n+1,
   dhy(1,j)=-(3*hh(1,j)-4*hh(2,j)+hh(3,j))/2/dy;
   for i=2:m
      dhy(i,j)=(hh(i+1,j)-hh(i-1,j))/2/dy;
   end;
   dhy(m+1,j)=0;
end;
for i=1:m+1,
```

```
   for j=1:n+1,
      f(i,j)=-1/pp(i,j)*(dpx(i,j)^2+(D/L)^2*dpy(i,j)^2)-
3/hh(i,j)*(dhx(i,j)*dpx(i,j)+dhy(i,j)*dpy(i,j))+mubar(j)*Lambda/hh(i,j)^2/pp(i,j)*dpx(i,j)
         +mubar(j)*Lambda/hh(i,j)^3*dhx(i,j);
      %f(i,j)=-1/pp(i,j)*(dpx(i,j)^2+(D/L)^2*dpy(i,j)^2)-(3/hh(i,j)*dhx(i,j)-
mubar(j)*Lambda/hh(i,j)^2/pp(i,j))*dpx(i,j)...
         %+mubar(j)*Lambda/hh(i,j)^3*dhx(i,j);
      %f(i,j)=mubar(j)*Lambda/hh(i,j)^3*dhx(i,j);
   end;
end;
ppn(1,:)=ones(1,n+1);
for i=2:m+1,
   for j=1:n+1
      if j==1
         if i==m+1
            ppn(i,j)=pp(i,j)+omega*((L/D)^2*dy^2*(pp(i-1,j)+pp(i-
1,j))+dtheta^2*(pp(i,j+1)+pp(i,n))...
               -2*(dtheta^2+(L/D)^2*dy^2)*pp(i,j)-
dtheta^2*(L/D)^2*dy^2*f(i,j))/(2*(dtheta^2+(L/D)^2*dy^2));
         else
            ppn(i,j)=pp(i,j)+omega*((L/D)^2*dy^2*(pp(i+1,j)+pp(i-
1,j))+dtheta^2*(pp(i,j+1)+pp(i,n))...
```

```
                -2*(dtheta^2+(L/D)^2*dy^2)*pp(i,j)-
dtheta^2*(L/D)^2*dy^2*f(i,j))/(2*(dtheta^2+(L/D)^2*dy^2));
        end;
    elseif j==n+1
        if i==m+1
            ppn(i,j)=pp(i,j)+omega*((L/D)^2*dy^2*(pp(i-1,j)+pp(i-
1,j))+dtheta^2*(pp(i,2)+pp(i,j-1))...
                -2*(dtheta^2+(L/D)^2*dy^2)*pp(i,j)-
dtheta^2*(L/D)^2*dy^2*f(i,j))/(2*(dtheta^2+(L/D)^2*dy^2));
        else
            ppn(i,j)=pp(i,j)+omega*((L/D)^2*dy^2*(pp(i+1,j)+pp(i-
1,j))+dtheta^2*(pp(i,2)+pp(i,j-1))...
                -2*(dtheta^2+(L/D)^2*dy^2)*pp(i,j)-
dtheta^2*(L/D)^2*dy^2*f(i,j))/(2*(dtheta^2+(L/D)^2*dy^2));
        end;
    else
        if i==m+1
            ppn(i,j)=pp(i,j)+omega*((L/D)^2*dy^2*(pp(i-1,j)+pp(i-
1,j))+dtheta^2*(pp(i,j+1)+pp(i,j-1))...
                -2*(dtheta^2+(L/D)^2*dy^2)*pp(i,j)-
dtheta^2*(L/D)^2*dy^2*f(i,j))/(2*(dtheta^2+(L/D)^2*dy^2));
        else
```

```
                ppn(i,j)=pp(i,j)+omega*((L/D)^2*dy^2*(pp(i+1,j)+pp(i-
1,j))+dtheta^2*(pp(i,j+1)+pp(i,j-1))...
                  -2*(dtheta^2+(L/D)^2*dy^2)*pp(i,j)-
dtheta^2*(L/D)^2*dy^2*f(i,j))/(2*(dtheta^2+(L/D)^2*dy^2));
           end
       end;
   end;
end;
pp_error=abs(norm(ppn)-norm(pp))
end;
return;
```

(4) Foil compliance

```
function [pp, hh1, dpx, dpy] = compliant(D, L, alpha, Lambda, epsilon, mubar, h, hh, pp,
m, n, dy, dtheta, theta);
for j=1:n+1,
  h1(j)=h(j)+alpha*(mean(pp(:,j))-1);
end;
for i=1:m+1,
  hh1(i,:)=h1;
end;
compliant_run=0;
factor=0.25;
while (abs(norm(hh1)-norm(hh))/abs(norm(hh1))>1e-3)
```

```
   hh=factor*hh1+(1-factor)*hh;
   [pp, dpx, dpy] = compres(D,L,Lambda,mubar,hh,pp,m,n, dy, dtheta);
   for j=1:n+1,
      h1(j)=h(j)+alpha*(mean(pp(:,j))-1);
   end;
   for i=1:m+1,
      hh1(i,:)=h1;
   end;
   compliant_run=compliant_run+1
end;
```

(5) Shaft movement (Eccentricity ratio change)

```
function [pp1, hh1, dpx, dpy, epsilon1] = eccentric(D, L, alpha, Lambda, epsilon, mubar,
h, hh, hh1, pp, pp1, m, n, dy, dtheta, theta);
h_change=alpha*(mean(pp1)-1);
epsilon_change=max(h_change);
for j=1:n+1,
   hh2(:,j)=hh1(:,j)+epsilon_change*cos(theta(j));
end;
epsilon_run=0;
factor=0.25;
while (abs(norm(hh2)-norm(hh1))/abs(norm(hh2))>1e-3)
   hh1=factor*hh2+(1-factor)*hh1;
   [pp1, dpx, dpy] = compres(D,L,Lambda,mubar,hh1,pp1,m,n,dy,dtheta);
```

```
    for j=1:n+1,
        h1a(j)=h(j)+alpha*(mean(pp1(:,j))-1);
    end;
    for i=1:m+1,
        hh1a(i,:)=h1a;
    end;
    h_change=alpha*(mean(pp1)-1);
    epsilon_change=max(h_change);
    for j=1:n+1,
        hh2(:,j)=hh1a(:,j)+epsilon_change*cos(theta(j));
    end;
    epsilon_run=epsilon_run+1
end;
epsilon1=epsilon+epsilon_change;
```

(6) Load calculation

```
function [Wr, phi] = load(pp,theta,dtheta,dy,p0,R,L,m,n);
for i=1:2*m+1
    cav(i)=n/2;
    while pp(i,cav(i))>1
        cav(i)=cav(i)+1;
    end;
    cav(i)=cav(i)-1;
    func4(i,1:cav(i))=(pp(i,1:cav(i))-1).*cos(theta(1:cav(i)));
```

```
    func5(i,1:cav(i))=(pp(i,1:cav(i))-1).*sin(theta(1:cav(i)));
    Wx(i)=Simps(func4(i,:),cav(i),dtheta);
    Wy(i)=Simps(func5(i,:),cav(i),dtheta);
end;
Wxx=(Simps(Wx,2*m+1,dy));
Wyy=(Simps(Wy,2*m+1,dy));
Wr=p0*R*L*sqrt(Wxx^2+Wyy^2);
phi=180*atan(-Wyy/Wxx)/pi;
```

(7) Numerical integration subroutine

```
function Q = Simpson(func, npoint, deltax);
panel=npoint-1;
half=panel/2;
Q=0;
i=1;
if (panel-2*half)~=0
    Q=3*deltax/8*(func(1)+3*func(2)+3*func(3)+func(4));
    i=4;
end;
Q=Q+deltax/3*(func(i)+4*func(i+1)+func(npoint));
i=i+2;
while i+2<=npoint
    Q=Q+deltax/3*(2*func(i)+4*func(i+1));
    i=i+2;
```

```
end;
```

(8) Flow rate calculation

```
function [Qleak, Qsuck, Qrec, P_mid, cav] = FlowRate(omega, R, D, L, C, p0, mu0,
mubar, pp1, hh1, dpx, dpy, m, n, dy, dtheta);
P_mid=pp1(m+1,:);
cav=n/2;
while P_mid(1,cav)>1
   cav=cav+1;
end;
cav=cav-1;
P_edge=pp1(2,:);
cav1=n/2;
while P_edge(1,cav1)>1
   cav1=cav1+1;
end;
cav1=cav1-1;
func1=hh1(1,1:cav1).^3.*dpy(1,1:cav1)./mubar(1:cav1);
Qleak=1/6*Simps(func1, cav1, dtheta);
func2=hh1(1,cav1+1:n+1).^3.*dpy(1,cav1+1:n+1)./mubar(cav1+1:n+1);
Qsuck=-1/6*Simps(func2, n+1-cav, dtheta);
for i=1:m+1
   cavm(i)=n/2;
   while pp1(i,cavm(i))>1
```

```
        cavm(i)=cavm(i)+1;
    end;
    cavm(i)=cavm(i)-1;
    func3(i)=hh1(i,cavm(i));
    func4(i)=hh1(i,cavm(i))^3*dpx(i,cavm(i));
end;
cavm_av=round(mean(cavm));
Qrec=mu0*R*omega*L^2/(4*p0*R*C^2)*Simps(func3,m+1,dy)-
(L/D)^2/(6*mubar(cavm_av))*Simps(func4,m+1,dy);
```

(9) Energy equation

```
function [Ts,Ti,T,rho1] = energy(KK, T0, H,tb,k,kb,omega, epsilon, R, C, p0, mu0,
mubar, h1, pp1, P_mid1, cav, Qleak, Qsuck, Qrec,kapa1,kapa2,kapa3, n, mn, dy, dtheta,
dz,z);
kapa4=C^2*p0/(2*mu0*omega*R^2)./mubar;
Nu=H*(R+tb+C*h1)/k;
for j=1:n,
    gama(j)=-(1/h1(j)*(R/C)+1)*(1/Nu(j)+k/kb*log(1+tb/(R+C*h1(j))));
end;
rho=ones(1,n+1);
[Ts,Ti,T] = Tshaft(rho,k, gama, Qleak, Qsuck, Qrec, P_mid1, cav, h1, kapa1, kapa2,
kapa3, kapa4, n, mn, dtheta, dz, z);
for j=1:n+1
    rho1(j)=P_mid1(j)/(1+(1-KK/T0)*mean(T(1:mn,j)));
```

```
end;
rho_run=0;
while abs(norm(rho1)-norm(rho))>1e-3
   rho=rho1;
   [Ts,Ti,T] = Tshaft2(rho,k, gama, Qleak, Qsuck, Qrec, P_mid1, cav, h1, kapa1, kapa2,
kapa3, kapa4, n, mn, dtheta, dz, z);
   for j=1:n+1
      rho1(j)=P_mid1(j)/(1+(1-KK/T0)*mean(T(1:mn,j)));
   end;
   rho_run=rho_run+1
end;
```

(10) Iteration on shaft temperature

```
function [Ts,Ti,T] = Tshaft(rho,k,gama, Qleak, Qsuck, Qrec, P_mid, cav, h1, kapa1,
kapa2, kapa3, kapa4, n, mn, dtheta, dz, z);
Ts=0;
[Ti,T] = Tmix(rho,Ts,gama, Qleak, Qsuck, Qrec, P_mid, cav, h1, kapa1, kapa2, kapa3,
kapa4, n, mn, dtheta, dz, z);
for j=1:n+1
   flux(j)=k*(T(mn-1,j)-Ts)/(2*dz);
end;
q=Simps(flux, n+1, dtheta);
Ts_run=0;
while (q>0)
```

```
    Ts=Ts+0.001;
    [Ti,T] = Tmix(rho,Ts,gama, Qleak, Qsuck, Qrec, P_mid, cav, h1, kapa1, kapa2, kapa3,
kapa4, n, mn, dtheta, dz, z);
    for j=1:n+1
        flux(j)=k*(T(mn-1,j)-Ts)/(2*dz);
    end;
    q=Simps(flux, n+1, dtheta);
    Ts_run=Ts_run+1
end;
```

(11) Iteration on inlet temperature

```
function [Ti,T] = Tmix(rho, Ts, gama, Qleak, Qsuck, Qrec, P_mid, cav, h1, kapa1, kapa2,
kapa3, kapa4, n, mn, dtheta, dz, z);
Ti=0;
T=marching(rho,Ts,Ti,gama,P_mid,h1,kapa1,kapa2,kapa3,kapa4,n,mn,dtheta,dz,z);
Qsup=Qleak;
Ti_run=0
Ti1=mean(mean(T(:,1:cav)))*Qrec/(Qrec+Qsup)
while abs(Ti1-Ti)/Ti1>1e-3;
    Ti_run=Ti_run+1
    Ti=Ti1;
    T=marching(rho,Ts,Ti,gama,P_mid,h1,kapa1,kapa2,kapa3,kapa4,n,mn,dtheta,dz,z);
    Ti1=mean(mean(T(:,1:cav)))*Qrec/(Qrec+Qsup)
end
```

(12) Marching technique

```
function T=marching(rho, Ts, Ti, gama, P_mid, h1, kapa1, kapa2, kapa3, kapa4, n, mn,
dtheta, dz, z);
P_mid=ones(1,n+1);
h=h1;
dx=dtheta;
dh(1)=-(3*h(1)-4*h(2)+h(3))/2/dx;
for j=2:n
  dh(j)=(h(j+1)-h(j-1))/2/dx;
end;
%dh(n+1)=-dh(1);
dp(1)=-(3*P_mid(1)-4*P_mid(2)+P_mid(3))/2/dx;
for j=2:n
  dp(j)=(P_mid(j+1)-P_mid(j-1))/2/dx;
end;
%dp(n+1)=dp(1);
ddpp(1)=((P_mid(3)-P_mid(1))/2/dx+(3*P_mid(1)-4*P_mid(2)+P_mid(3))/2/dx)/dx;
for j=2:n
  ddpp(j)=(P_mid(j+1)-2*P_mid(j)+P_mid(j-1))/dx^2;
end;
%ddpp(n+1)=ddpp(1);
for j=1:n+1
  T(mn+1,j)=Ts;
```

```
end;
for i=1:mn
  T(i,1)=Ti;
end;
for j=1:n-1,
  for i=1:mn;
      u(i)=(z(i)+kapa4(j)*(z(i)^2-z(i))*h(j)^2*dp(j));
      du(i)=(1+kapa4(j)*(2*z(i)-1)*h(j)^2*dp(j));
      w(i)=-kapa4(j)*(2*h(j)^2*dh(j)*dp(j)+h(j)^3*ddpp(j))*(z(i)^3/3-z(i)^2/2);
      if u(i)<0,
         u(i)=-u(i);
         a(i)=-(kapa1/kapa2^2/(h(j)^2*rho(j)*dz^2)...
            +(w(i)-z(i)*u(i)*dh(j))/(2*h(j)*dz));
               b(i)=2*kapa1/kapa2^2/(h(j)^2*rho(j)*dz^2)+1/dx*u(i)-
kapa1/(h(j)^2*rho(j))*(du(i))^2;
         c(i)=-(kapa1/kapa2^2/(h(j)^2*rho(j)*dz^2)...
            -(w(i)-z(i)*u(i)*dh(j))/(2*h(j)*dz));
         d(i)=1/dx*u(i)*T(i,j)+kapa3*u(i)*(-dp(j))/rho(j)+kapa1/(h(j)^2*rho(j))*(du(i))^2;
      else
         a(i)=-(kapa1/kapa2^2/(h(j)^2*rho(j)*dz^2)...
            +(w(i)-z(i)*u(i)*dh(j))/(2*h(j)*dz));
               b(i)=2*kapa1/kapa2^2/(h(j)^2*rho(j)*dz^2)+1/dx*u(i)-
kapa1/(h(j)^2*rho(j))*(du(i))^2;
```

```
            c(i)=-(kapa1/kapa2^2/(h(j)^2*rho(j)*dz^2)...
                -(w(i)-z(i)*u(i)*dh(j))/(2*h(j)*dz));
            d(i)=1/dx*u(i)*T(i,j)+kapa3*u(i)*(dp(j))/rho(j)+kapa1/(h(j)^2*rho(j))*(du(i))^2;
        end;
    end;
    b(1)=a(1)*2*dz/gama(j)+b(1);
    c(1)=a(1)+c(1);
    A=zeros(mn,mn);
    for k=1:mn-1
        A(k,k)=b(k);
        A(k+1,k)=a(k+1);
        A(k,k+1)=c(k);
    end;
    A(mn,mn)=b(mn);
    d(mn)=d(mn)-c(mn)*Ts;
    coeff=inv(A)*d';
    T(1:mn,j+1)=coeff;
    %rho(j+1)=P_mid(j+1)/(1+(1-KK/T0)*mean(T(1:mn,j+1)));
end;
T(1:mn,n+1)=Ti;
```

VITA

The author of this thesis was born in March 1974 at Chongqing, China. In 1996, he received his Bachelor of Science in Vehicle Engineering at Beijing Institute of Technology. He then came to United States in 2000 to study Mechanical Engineering at Louisiana State University under the supervision of Prof. Michael Khonsari. He will graduate in May 2003 with the degree of Master of Science in Mechanical Engineering.